Airborne Measurements of Scale-Dependent Latent Heat Flux Impacted by Water Vapor and Vertical Velocity over Heterogeneous Land Surfaces During the CHEESEHEAD19 Campaign

Guo Lin[1,2], Zhien Wang[1,2*], Yufei Chu[1,2], Conrad Ziegler[3,4], Xiao-Ming Hu[4,5], Ming Xue[4,5], Bart Geerts[6], Sreenath Paleri[7], Ankur R. Desai[7], Kang Yang[1,2], Min Deng[8], and Jonathan DeGraw[4,5]

[1]*Department of Atmospheric and Oceanic Sciences, University of Colorado Boulder, Boulder, Colorado*
[2]*Laboratory for Atmospheric and Space Physics, University of Colorado Boulder, CO*
[3]*NOAA/National Severe Storms Laboratory, Norman, OK*
[4]*School of Meteorology, University of Oklahoma, Norman, OK*
[5]*Center for Analysis and Prediction of Storms, University of Oklahoma, Norman, OK*
[6]*Department of Atmospheric Science, University of Wyoming, Laramie, WY*
[7]*Department of Atmospheric and Oceanic Sciences, University of Wisconsin-Madison, Madison, WI*
[8]*Environmental and Climate Sciences Department, Brookhaven National Laboratory, Upton, NY*

To be submitted to *JGR: Atmospheres*
Date: July 2023

[*]Corresponding author: Zhien Wang (Zhien.Wang@colorado.edu)
Laboratory for Atmospheric and Space Physics and Department of Atmospheric and Oceanic Sciences, University of Colorado Boulder, 3665 Discovery Dr., Boulder, CO 80303.

Key Points

- The scale-dependent distribution of latent heat flux, vertical velocity variance, and water vapor variance at 100 m over a heterogeneous surface is described.
- In the large-eddy scale, 69 to 75 % of total latent heat flux is contributed by 32-45% of total vertical velocity variance and 35-55 % of total water vapor variance.
- The large-eddy scale contributes most of the vertical moisture transport from the surface to the Planetary Boundary Layer.

Abstract

The spatiotemporal variability of latent heat flux (LE) and water vapor mixing ratio (r_v) variability are not well understood due to the scale-dependent and nonlinear atmospheric energy balance responses to land surface heterogeneity. Airborne in situ and profiling Raman lidar measurements with the wavelet technique are utilized to investigate scale-dependent relationships among LE, vertical velocity (w) variance (σ^2_w), and r_v variance (σ^2_{wv}) over a heterogeneous surface in the Chequamegon Heterogeneous Ecosystem Energy-balance Study Enabled by a High-density Extensive Array of Detectors 2019 (CHEESEHEAD19) field campaign. Our findings reveal distinct scale distributions of LE, σ^2_w, and σ^2_{wv} at 100 m height, with a majority scale range of 120 m-4 km in LE, 32 m - 2 km in σ^2_w, and 200 m – 8 km in σ^2_{wv}. The scales are classified into three scale ranges, the turbulent scale (8 m – 200 m), large-eddy scale (200 m–2 km), and mesoscale (2 km – 8 km) to evaluate scale-resolved LE contributed by σ^2_w and σ^2_{wv}. In the large-eddy scale in Planetary Boundary Layer (PBL), 69-75% of total LE comes from 31-51% of the total σ_w and 39-59% of the total σ^2_{wv}. Variations exist in LE, σ^2_w, and σ^2_{wv}, with a range of 1.7-11.1% of total values in monthly-mean variation, and 0.6–7.8% of total values in flight legs from July to September. These results confirm the dominant role of the large-eddy scale in the PBL in the vertical moisture transport from the surface to the PBL. This analysis complements published scale-dependent LE variations, which lack detailed scale-dependent vertical velocity and moisture information.

Plain Language Summary

The vertical water vapor transport in the planetary boundary layer (PBL), and the associated latent heat flux (LE), are critical for the atmospheric hydrological cycle, radiation balance, and cloud formation. However, the vertical moisture transport varies nonlinearly at multiple scales due to the land surface heterogeneity across multiple properties. This study investigates the scale-resolved impact of water vapor and vertical velocity on LE, using data collected aboard an atmospheric research aircraft flying low above the surface in summer over northern Wisconsin during the CHEESEHEAD19 campaign. This study finds that LE and water vapor variance is largest at the large-eddy scale in PBL and at the mesoscale. In contrast, vertical velocity variance is primarily present in turbulent and large-eddy scales in PBL. This study confirms the significant role of the large-eddy scale in PBL in contributing to the majority of the vertical moisture transport from the surface to the PBL top. These findings provide better insight into the factors influencing LE at different scales.

1. Introduction

Water vapor and latent heat flux (LE) in the Planetary Boundary Layer (PBL) play critical roles in atmospheric dynamics, the hydrological cycle, radiation balance, and conversion of latent heat (Garratt, 1994; Pielke et al., 2003; Linné et al., 2006; Kiemle et al., 2007; Stevens & Bony, 2013; Stull, 2015; Hu et al., 2023). Relevant processes include surface evapotranspiration, transport and diffusion through the PBL, and cloud formation and dissipation (LeMone et al., 2019). The PBL, where the mixing process by turbulent eddies at different scales plays a critical role, transports water vapor from the surface to the free atmosphere. LE in the PBL is derived from the surface, through evapotranspiration, modulated by the entrainment of air in the free troposphere, and PBL circulation and evolution (Linné et al., 2006). However, the land surface heterogeneity across multiple properties drives spatial variability of the vertical transport at various scales in a nonlinear fashion (Raupach & Finnigan, 1995; Avissar & Schmidt, 1998; Platis et al., 2017). Depending on the relative magnitude of the surface and entrainment fluxes, the idealized water vapor flux profile within the well-mixed convective boundary layer (CBL) either decreases or increases with height, in a linear fashion (Stull, 1988). Bange et al. (2002), investigating heat fluxes using airborne flux measurements in the CBL, found linear profiles of sensible heat flux but not LE. Water vapor and LE measurements are crucial to understanding water vapor transport and its variability in PBL. Although the importance of water vapor is well recognized, its spatial and temporal variability is still poorly characterized by observations, making model validation difficult (Linné et al., 2006; Eder et al., 2015; Wolf et al., 2017; Bou-Zeid et al., 2020; Mauder et al., 2020; Butterworth et al., 2021; Metzger et al., 2021). Accurate accounting of land-atmosphere interactions is critical for improving the performance of numerical weather and climate models.

Water vapor variability on scales comparable to the finest resolution of climate and weather models is not yet well characterized and understood due to the atmospheric responses from energy balance on land surface heterogeneity, despite its significant influence on the development of cloud and precipitation processes (Sherwood et al., 2010; Wang et al., 2010). The land surface is usually heterogeneous over a wide range of spatial scales due to variability in, among other parameters, vegetation, terrain, soil texture and wetness, cloud cover, and urban

areas (Mahrt, 2000; Desai et al., 2005; Desai et al., 2022b). However, measurements at a single location, such as eddy correlation flux towers, are often used to represent the properties of a larger region. Individual point sensors may not be representative in complex terrain or in varied vegetation (Bou-Zeid et al., 2020; Mauder et al., 2020; Butterworth et al., 2021).

While most horizontal humidity transport occurs through advection on large scales and is well resolved in atmospheric models, vertical transport is dominated by turbulence on sub-grid scales and must be parameterized (Kiemle et al., 2007). The vertical transport of water vapor generated by surface forcings from the heterogeneous land surface at multiple scales leads to scale-dependent atmospheric variability (Avissar & Schmidt, 1998). Water vapor is a complex natural multiscale phenomenon that requires scale-based parameterizations because it is hard to resolve all the relevant spatial information directly in numerical simulations or through observations (Pressel et al., 2014). The lack of understanding of the small-scale dynamics of water vapor throughout the PBL leads to strong limitations in predicting localized phenomena in weather models (Couvreux et al., 2005; Steinfeld et al., 2007; Hill et al., 2008; Hill et al., 2011). As such, the multiscale nature of water vapor has continued to defy a generalized approach or theory for "characterizing" its impact on the PBL (Mahrt, 2000). Heat and moisture exchange measurements between the land surface and the atmosphere are critical to understanding the causes of variability in the PBL.

The eddy covariance (EC) technique is widely used to estimate the energy exchange between the surface and the atmosphere at a single location: water vapor fluxes are estimated from the covariance of the water vapor and vertical velocity perturbations (Aubinet et al., 2012). The water vapor flux (g kg^{-1}m s^{-1}) is the covariance of w (m s^{-1}) and r_v (g kg^{-1}). This flux translates into the LE (W m^{-2}) by multiplying the air density and the latent heat of water vaporization. The LE is a valuable tool for monitoring changes in local sources and sinks of water vapor subjected to local influences at a fixed station over an extended period. The EC technique suffers from certain limitations in covering the full spectrum of the atmospheric transport (Finnigan et al., 2003; Mauder et al., 2007). A sufficiently long averaging interval is required to minimize the spectral loss in the low-frequency part. Non-local mesoscale eddies might either be geographically fixed to a surface heterogeneity, or slowly moving in weak wind conditions

(Mahrt, 1998). Traditional EC calculation approaches are usually inadequate for capturing mesoscale features associated with the surface heterogeneity (Foken et al., 2011; Charuchittipan et al., 2014; Gao et al., 2016; Butterworth et al., 2021).

Spatial sampling coverage from micro-γ scale (<20m) to meso-β scale (up to 200 km) can be provided by high-frequency instruments aboard aircraft flying in the surface layer. (the scale classification is based on Orlanski, 1975; Mauder et al., 2007; Paleri et al., 2022). Aircraft can fly a long distance to cover mesoscale eddies during one flight which is favorable for investigating atmospheric mesoscale motions whereas ground-based systems passively detect eddies brought by the mean wind (Mauder et al., 2007). The airborne measurement offers the advantage of reduced measurement time and increased sampling compared to ground-based in situ tower measurements (Desjardins et al., 1995). Recent projects with airborne flux measurements include the Boreal Ecosystem-Atmosphere Study (BOREAS; Sellers et al., 1995), the Northern Hemisphere Climate Processes Land-Surface Experiment (NOPEX; Halldin et al., 1999), the Lindenberg Inhomogeneous Terrain – Fluxes between Atmosphere and Surface: a Long-term Study (LITFASS-98; Beyrich et al., 2002) and LITFASS-2003 (Beyrich & Mengelkamp, 2006), MAtter fluxes in Grasslands of Inner Mongolia as influenced by stocking rate (MAGIM; Butterbach-Bahl et al., 2011), and ScaleX (Wolf et al., 2017). The airborne estimation of LE is based on the combination of water vapor with vertical velocity measurements using the EC technique (Linné et al., 2006) and wavelet technique (Mauder et al., 2007; Metzger et al., 2013; Paleri et al., 2022). Mauder et al. (2007) found that the differences between these techniques are relatively small, especially less than 2% for LE between the EC and wavelet techniques. Differences between aircraft and tower-based estimates of water vapor fluxes are often much larger (Desjardins et al. (1997). Aircraft can serve as extended observation platforms for the scaling up from local (tower-based) to regional estimates of surface-atmosphere energy exchange (Butterworth et al., 2021; Metzger et al., 2021). Although airborne measurements have limitations in sampling duration, frequency, and distance due to operational considerations and high costs (Desjardins et al., 1997; Mauder et al., 2007), the airborne EC measurements are suitable for characterizing the water vapor and LE variability in a targeted experiment.

Here, we characterize the scale-dependence of LE, vertical velocity (w) variance (σ^2_w), and water vapor (r_v) variance (σ^2_{wv}) at the 100 m above ground level (AGL) flight level in the Chequamegon Heterogeneous Ecosystem Energy-Balance Study Enabled by a High-Density Extensive Array of Detectors 2019 (CHEESEHEAD19) campaign (Butterworth et al. 2021). The objective is to investigate the spatial-dominant scale of LE, σ^2_w, and σ^2_{wv} in the lower PBL and how σ^2_w and σ^2_{wv} impact LE variability on diurnal to seasonal scales. Our study examines three hypotheses on scaled-dependent LE, measured within the PBL during the daytime, based on the literature discussed above:

H1: The spectral characteristics of σ^2_w and σ^2_{wv} are different.

H2: σ^2_w generated by the surface is concentrated across scales less than the PBL height, which is normally below 2 km.

H3: The scale-dependent σ^2_{wv} includes the contributions of the entrainment of dry air from the free troposphere, and PBL circulation and evolution, which are in large-eddy scale in PBL and even mesoscale.

Ultimately, by contrasting the contributing spatial scales of the LE, σ^2_w, and σ^2_{wv}, this study leads to a more accurate quantitative assessment of spatially localized contributions from all the relevant transport scales. Section 2 introduces the CHEESEHEAD19 field campaign and reviews the data collection methods, datasets, and instruments. The temporal and spatial variability of LE and how σ^2_w and σ^2_{wv} impact are detailed in Section 3, while discussion and conclusions are presented in Section 4 and Section 5.

2. Data and Methodology

2.1 Experimental Procedure

The CHEESEHEAD19 was an intensive field campaign supported by the National Science Foundation in the Chequamegon-Nicolet National Forest of Wisconsin from June to October 2019 (Butterworth et al., 2021). The experiment was designed to intensively sample land–surface properties and the BL responses to surface properties across a heterogeneous mid-latitude forested landscape. The land cover within the CHEESEHEAD19 domain is dominated by conifers, deciduous forest, mixed forest, wetlands, and open water, according to the National Land Cover Database (NLCD) 2019 land cover (Figure 1; Dewitz & U.S. Geological Survey, 2021). The canopy heights range from 0 to 35 meters, leading to a horizontally heterogeneous surface. This forest, with diverse surface properties varying at multiple scales, was selected to address a crucial gap in our current understanding of surface atmospheric exchanges over a heterogenous flat land surface (Bou-Zeid et al., 2020). Measurements of CHEESEHEAD used a suite of observing platforms over a core 10 x 10 km^2 domain (the red dashed domain in Figure 1a) and a 30 km x 30 km extended domain for airborne measurements. The study domain was partly chosen due to the history of atmospheric science research in the region (Davis et al., 2003; Desai et al., 2022a). The EC tower network consisted of 17 flux towers from the National Center for Atmospheric Research (NCAR) - Integrated Surface Flux Station (ISFS) network (colored circles in Figure 1), two additional contributed towers in grassland and a lake, and the tall Department of Energy Ameriflux regional tower (US Pfa/WLEF; the star in Figure 1) (Desai, 2023). A majority of the ISFS sites had flux instruments mounted at 33 m AGL for forests while instruments for wetland, grass, and lake sites were mounted between 1 and 3 m AGL to maintain consistent sampling within homogenous flux footprints (Oncley, 2021). The US PFa tower has sampled greenhouse gas profiles, meteorological data, and EC flux measurements (energy, carbon, momentum) at 30, 122, and 396 m above ground level (AGL) since 1995 (Berger et al., 2001; Davis et al., 2003). The fluxes can be simultaneously measured at seventeen points with tower-based systems and short periods with airborne measurements during Intensive Observation Periods (referred to as IOPs henceforth). Thus, the temporal and spatial characteristics of ground-based and airborne measurements complement each other to evaluate land-atmosphere

interactions in PBL at the site and regional scales (Butterworth et al., 2021; Hu et al., 2021; Paleri et al., 2022).

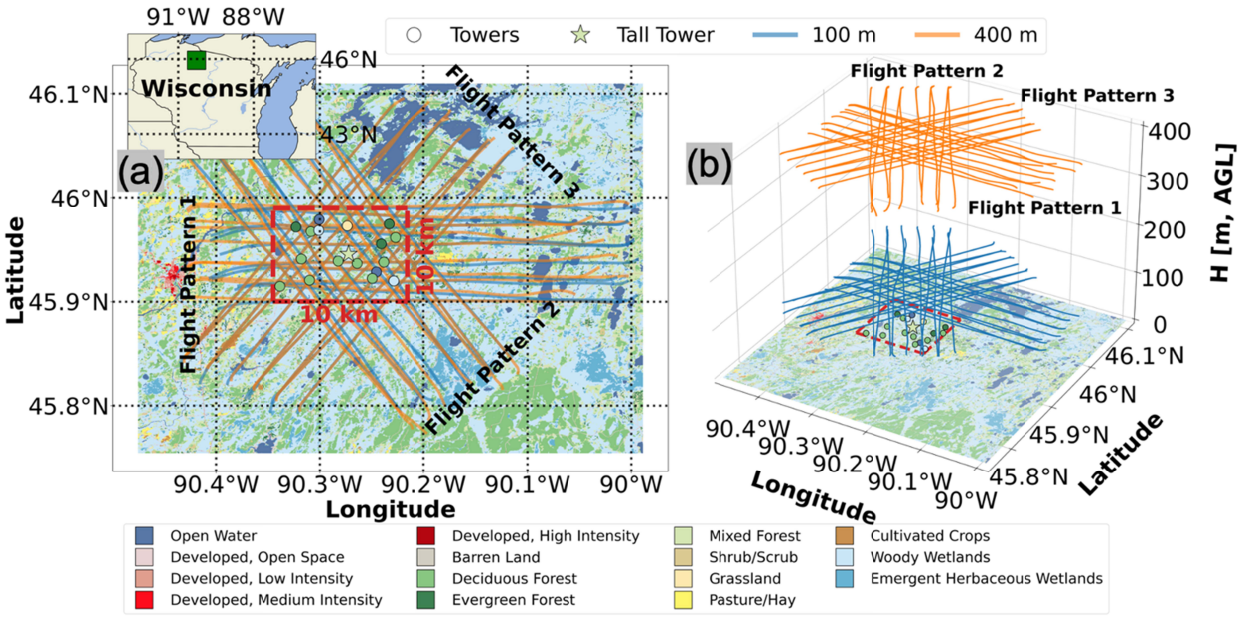

Figure 1. (*a) Location of the CHEESEHEAD19 domain (blue square) in Wisconsin (insert map) and colored land classification map from the NLCD 2019 of the area around the CHEESESHEAD19 domain with three distinct University of Wyoming King Air (UWKA) flight patterns at 100 m (blue lines) and 400 m (orange lines); (b) 3D map showing the three UWKA flight patterns at 100 m (blue lines) and 400 m (orange lines). The red dashed square represents the study domain of flux towers, and the dots and a star indicate the flux tower locations colored by their land cover types.*

2.2 Airborne Observations

The airborne observations aimed to examine PBL responding to spatial heterogeneous land cover. The University of Wyoming King Air (UWKA) aircraft was equipped a suite of atmospheric measurement probes, including wind, temperature, and humidity measurements up to 25 Hz to estimate turbulent fluxes (French et al., 2021). The UWKA used a high-precision geo-positioning system (Trimble/Applanix, model POS AV410) and gust probe to obtain 3D position and 3D velocity information, including horizontal wind speed (*Wspd*), horizontal wind direction

(*Wdir*), and *w* used in this study (Haimov & Rodi, 2013). The r_v is measured by LI-COR LI-7000 CO2/H2O analyzer. The sampling frequency of *w* and r_v is 25 Hz, and the aircraft flew at a true air speed of ~90 m/s. Net radiation (*Rnet*) data were also collected to provide information on theoretical maximum latent plus sensible heat fluxes. The UWKA also sampled 2D vertical profiles of water vapor, aerosols, and temperature below the flight level using a nadir-pointing Compact Raman Lidar (CRL; Liu et al., 2014; Wu et al., 2016; Lin et al., 2019; Lin et al., 2023) and aerosols with the zenith-pointing Wyoming Cloud Lidar (Wang et al., 2009; Lin et al., 2021) at 400 m height. Three IOPs with the UWKA were conducted during the experiment in each month from July to September (details in Table 1). The flight consisted of two 3-h flights for each research flight (RF in Table 1), one in the morning (1400–1700 UTC; odd numbers in RF, using M as morning) and another in the afternoon (1900–2200 UTC; even numbers in RF, using A as afternoon). The flight times relative to sunrise and sunset differ in RFs and months (Table 1). Three flight patterns (FPs) were conducted in IOPs (oriented W–E for FP1; NW-SE for FP2, SW–NE for FP3 in Figure 1 and Table 1) based on a flux heterogeneity optimization approach (Metzger et al., 2021).

Table 1. *IOPs, dates (The M represents morning and A represents afternoon), RF numbers and times, sunrise and sunset times, flight patterns, flight-level winds, and net radiation of all IOPs.*

IOP (#)	Date	Flight (#)	Time Period (Mor, UTC)	Time Period (Aft, UTC)	Sunrise (UTC)	Sunset (UTC)	Fight Pattern	Wspd (ms^{-1})	Wdir (deg)	Rnet (Wm^{-2})
	9 July M	RF 01	1413 – 1616		1121		FP1	6.4	278	495
	9 July A	RF 02		1919 – 2119		2646	FP1	4.6	271	540
	11 July M	RF 03	1429 – 1635		1122		FP1	2.9	102	658
IOP	11 July A	RF 04		1922 – 2127		2644	FP1	6.0	319	633
01	12 July M	RF 05	1358 – 1606		1123		FP1	6.0	318	539
	12 July A	RF 06		1841 – 2045		2644	FP1	6.2	347	528
	13 July M	RF 07	1428 – 1631		1124		FP2	5.1	44	626
	13 July A	RF 08		1917 – 2115		2643	FP3	3.7	71	648
	20 Aug M	RF 09	1358 – 1611		1206		FP2	6.2	262	164
	20 Aug A	RF 10		1931 – 2150		2556	FP2	3.0	150	502
	21 Aug M	RF 11	1415 – 1635		1207		FP3	4.7	40	524
IOP	21 Aug A	RF 12		1918 – 2137		2555	FP3	6.0	49	479
02	22 Aug M	RF 13	1417 – 1639		1208		FP3	2.6	134	320
	22 Aug A	RF 14		1921 – 2146		2553	FP3	4.4	116	274
	23 Aug M	RF 15	1414 – 1637		1209		FP1	3.4	159	509
	23 Aug A	RF 16		1925 – 2145		2551	FP1	4.3	184	536

	24 Sep M	RF 17	1359 – 1635		1247		FP2	6.4	260	356
	24 Sep A	RF 18		1919 – 2139		2452	FP2	6.9	280	244
	25 Sep M	RF 19	1448 – 1708		1248		FP3	7.6	8	433
IOP	25 Sep A	RF 20		1936 – 2152		2450	FP3	9.2	343	159
03	26 Sep M	RF 21	1413 – 1634		1250		FP2	4.4	278	359
	26 Sep A	RF 22		1852 – 2114		2448	FP2	7.2	338	314
	28 Sep M	RF 23	1444 – 1705		1252		FP1	3.2	104	464
	28 Sep A	RF 24		1915 – 2134		2444	FP1	4.0	107	349

During the UWKA RFs, the aircraft flew a ~30 km leg at 400 m AGL (orange flight tracks in Figure 1) to sample the temperature, aerosols, and moisture profiles of the PBL with the CRL. The UWKA then flew a ~30 km leg back at 100 m AGL (orange flight tracks in Figure 1) to measure turbulent fluxes at flight level. The 400 m and 100 m flights were repeated ten times in every RF. The 100 m altitude is the lowest altitude deemed safe to fly within the surface layer as the canopy height extends to 35m. The choice of FP was based on the prevailing wind direction: the one closest perpendicular to the prevailing wind was chosen (Metzger et al., 2021). The flight legs extended an average of 10 km beyond the core domain to maximize data coverage under different wind conditions and the number of independent atmospheric eddies observed by the aircraft EC measurements. The 30 km flight legs captured enough eddies and mesoscale variation to properly compute eddy correlation statistics for fluxes using the wavelet decomposition method (Mauder et al., 2007; Paleri et al., 2022). Although the CHEESEHEAD19 dataset provided good spatial coverage but with limited temporal coverage (72 flight hours in 12 days, all with fair-weather conditions), it is still one of the largest airborne flux measurement datasets collected to date.

2.3 Wavelet Flux Analysis

A wavelet transform can be used to evaluate the scale-depended contribution of atmospheric fluxes from aircraft measurements (Attié & Durand, 2003; Strunin & Hiyama, 2005; Mauder et al., 2007; Vadrevu & Choi, 2011; Paleri et al., 2022). The wavelet functions and analysis methods were developed for time-frequency analysis revealing localized information (Farge, 1992; Thomas & Foken, 2004). The wavelet analysis is a powerful mathematical tool that, based on the ergodic hypothesis, does not require data to be stationary at many different frequencies (Torrence & Compo, 1998; Strunin & Hiyama, 2005; Mauder et al., 2007), unlike other

conventional methods such as a Fourier transform (Foken & Wichura, 1996). In this regard, the wavelet analysis is particularly suitable for aircraft data measured above heterogeneous terrain to calculate atmospheric fluxes on different scales during the CHEESEHEAD19 field campaign. The existing wavelet methodology is expanded to facilitate space-scale analysis of the UWKA in-situ data from Torrence and Compo (1998) and (Mauder et al., 2007). The Morlet wavelet has been selected as the mother wavelet in the field of atmospheric turbulent studies, because of its good localization in space and frequency domains (e.g., Torrence & Compo, 1998; Mauder et al., 2007; Paleri et al., 2022). The wavelet equations of the wavelet power spectrum, variance, power co-spectrum, and covariance are described in detail in the Supplement. The wavelet spectrum and co-spectrum depend on the scale-dependent bin size, but variance (Equation S7) and covariance (Equation S11) are independent of bin size, since they are normalized by bin size. Mauder et al. (2007) show examples of covariance calculated by the wavelet technique from airborne in situ measurements and scale-resolved distributions in their Figure 4. In this study, the wavelet technique is used to calculate and evaluate the 100 m flight-level scale-resolved distribution and temporal variation of LE, σ^2_w, and σ^2_w for all flight legs from the July, August, and September IOPs (Table 1). The normalized scale-resolved LE, σ^2_w, and σ^2_w calculated by Equations S10 and S12 are used to analyze the relative scale-dependent contribution from σ^2_w and σ^2_w to LE regardless of their values.

2.3.1 Example of Wavelet Variance and Covariance

The wavelet method permits to allocate the information about flux contributions from the entire flight track to a specific subsegment of that track. We apply wavelet calculation to the same flight track of Figure 3 in Paleri et al. (2022) for comparison and to ensure consistent calculation (Figure 2). The wavelet analysis is applied to calculate the wavelet power co-spectrum of LE, and the wavelet power spectra of w and r_v (Figures 2a-c). We also calculated LE using Equation S11, and σ^2_w (m^2s^{-2}) and σ^2_{wv} ($g^2\ kg^{-2}$) using Equation S7 with 100 m flight-level data for spatial and scale analysis (Figures 2d-i). The hashed areas shown in Figures 2a-c are the cone of influence (COI) where edge effects due to discontinuities at the endpoints become important. Since the wavelet decomposition deals with finite-length flight leg, errors will occur at the beginning and end of the wavelet power spectrum (Torrence & Compo, 1998).

311

312 Spatial variations of LE, σ^2_w, and σ^2_{wv} were calculated by normalizing power spectra and the co-
313 spectrum with scale-dependent bin size and integrating the scale up to 8 km along the flight-track
314 segment (Figures 2d-f) since the integrated processes covering the full-range scale may introduce
315 uncertainties by the COI. The spatial LE, σ^2_w, and σ^2_{wv} are smoothed by 28-point average
316 windows (100m; blue lines), and 278-point averaged windows (1km; orange lines in Figure 2d-f).
317 The 1 km window-averaged LE varies from 60 to 600 Wm^{-2} in a 28 km flight track. The land
318 classification is mapped out at the bottom of Figures 2d-f. The spatial LE is related to surface
319 heterogeneity, with the lowest LE occurring at 18 km over water along the flight track. The
320 maximum 600 Wm^{-2} latent heat flux at 9 km coincides with the cross-scalogram of LE power
321 contribution up to 4 km (Figure 2a). However, the high value of LE does not correlate to only
322 high σ^2_w or high σ^2_{wv}, but instead to the covariance of σ^2_w and σ^2_{wv}. The 600 Wm^{-2} LE at around
323 9 km is collocated with 1.3 m^2s^{-2} σ^2_w and 0.12 g^2kg^{-2} σ^2_{wv}. Neither σ^2_w nor σ^2_{wv} is the maximum
324 value in the segment.
325

326 The spatial variations (Figure 2d-f) along the flight-track segment cannot resolve the scale
327 contribution of σ^2_w and σ^2_{wv} to LE clearly. The leg-averaged scale-resolved LE (Figure 2g)
328 reflects the importance of small-scale contributions with values greater than 2 Wm^{-2} in scales
329 from 100 m to 3 km with a maximum LE of 14 Wm^{-2} at ~0.4 km. The scale-resolved σ^2_w with
330 values greater than 5 x 10^{-2} m^2s^{-2} is between 16 m and 1.5 km within PBL turbulence scales (< 2
331 km; Figure 2b). The scale-resolved σ^2_{wv} is concentrated between 200 m and 8 km with a peak of
332 3.2 x 10^{-2} g^2kg^{-2} at 1 km. The distribution of scale-resolved σ^2_{wv} between 200 m and 8 km could
333 result from large-eddy circulations in PBL and mesoscale forcings. To see the scale-resolved σ^2_w
334 and σ^2_{wv} contributing to the scale-resolved LE, the scale-resolved covariance between w' and r_v'
335 ($cov_{(w,wv)}$) is calculated using Equation S13. The $cov_{(w,wv)}$ is shown in Figures 2g-i to compare the
336 different scale-resolved distributions among LE, σ^2_w, and σ^2_{wv}.
337

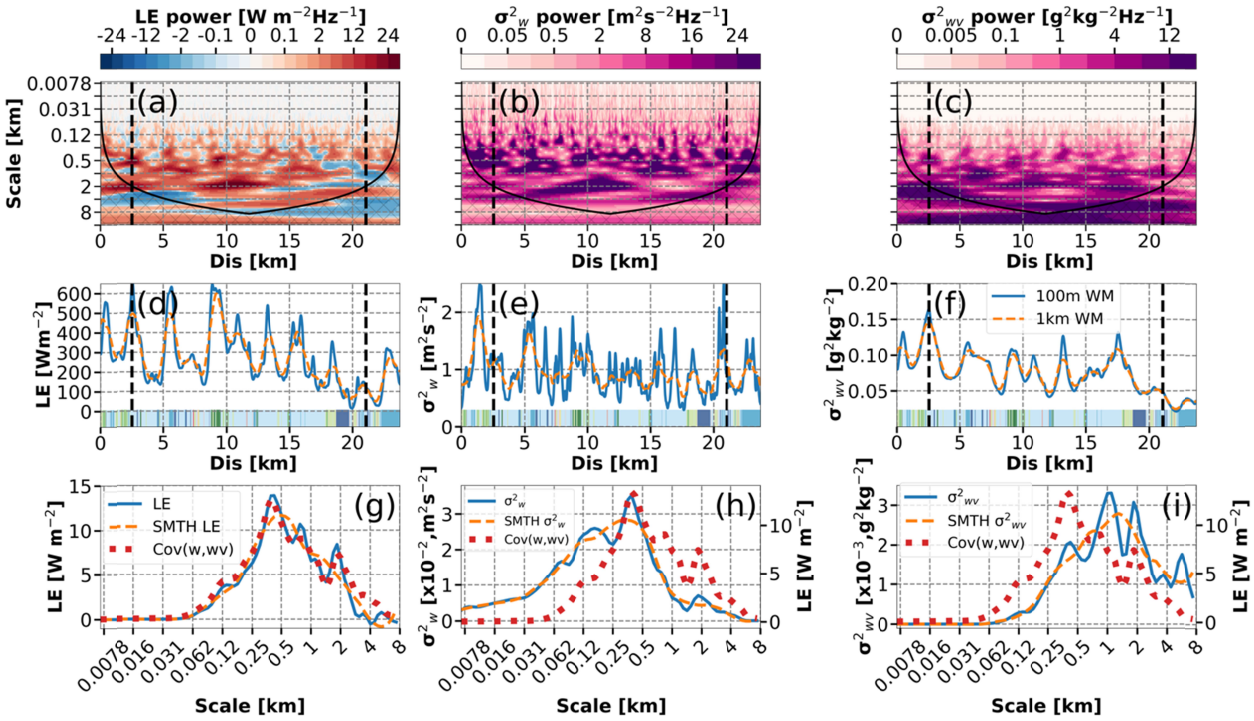

Figure 2. *A sample wavelet cross-scalogram between w and r_v in the result of (a) LE power; the wavelet scalogram of (b)* σ^2_w *power and (c)* σ^2_{wv} *power illustrating the scale-resolved spatial contributions along RF02 flight leg 2 at 100m AGL. The (d) scale-integrated LE, (e)* σ^2_w*, and (f)* σ^2_{wv} *along the flight tracks are calculated by integrating scalogram in spatial scales along the y-axis of panels a, b, and c, respectively. The (g) scale-dependent LE, (h)* σ^2_w *and (i)* σ^2_{wv} are *averaged over the flight leg between 2.5 km < x < 21 km (within two vertical black lines shown in panels a-f). Hashed portions in (a-c) below the black line represent the COI of edge effects. The vertical black lines represent the threshold of 2km influenced by COI for the chosen flight segment to calculate scale-dependent LE,* σ^2_w*, and* σ^2_{wv}*. The colored land classification map along the flight track is shown at the bottom of (d)-(f).*

2.3.2 Wavelet and Eddy Covariance LEs Comparison

To examine the accuracy of wavelet-calculated airborne LEs at 100 m, the flight-leg averaged LEs of 240 flight legs calculated by the wavelet technique are compared with leg-averaged LEs from the traditional EC technique (Figure 3a). Since the influence of edge effects by COI is generally larger towards the ends of the wavelet cross-scalogram (Figure 2a), a threshold of chosen segment legs is in the scale of COI greater than 2 km to ensure a long-enough fight leg to

sample mesoscale eddies and to reduce significant edge effects from discontinuities at the endpoints for wavelet LE calculations (i.e., the flight segment between two vertical black lines in Figure 2a). The traditional leg-averaged EC LE is defined (Stull, 1988):

$$EC\ LE = \overline{w' r_v'} \quad (1)$$

where w' and r_v' are the w perturbation and r_v perturbation from leg-averaged values, respectively. The same flight segment is used for LE calculations with the two techniques. The 2D histogram comparing traditional leg-averaged EC LEs against wavelet LEs for the 240 flight legs, shown in Figure 3a, has a bin size of 20 Wm^{-2} from 0 to 400 Wm^{-2}. The wavelet LE is slightly smaller than the EC LE with a mean bias error (MBE) of 4.85 Wm^{-2}, ~ 3.2% of the total mean EC LE, and the root mean square error (RMSE) of 30 Wm^{-2}. The correlation coefficient (r^2) is 0.915. The low mean differences and high r^2 indicate reliable leg-averaged wavelet LE compared to the EC LE.

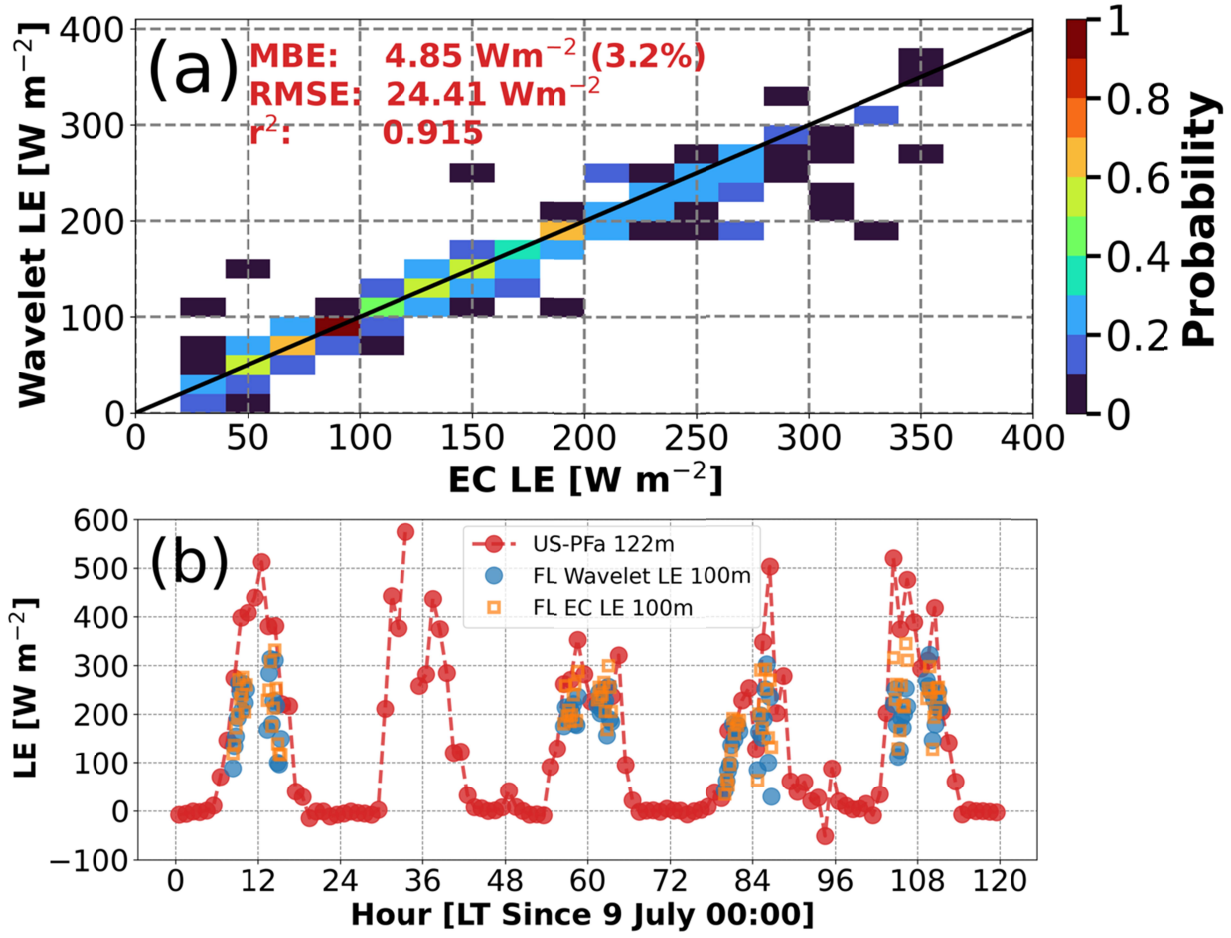

Figure 3. *(a) Comparison of airborne flight-level LEs calculated by the EC technique and the wavelet technique for all 100 m flight legs during all three IOPs (Table 1) ; (b) comparison of leg-averaged LEs at 100m flight level and LE at 122 m on the US PFa tall tower for the July IOP. The flight-level LE is calculated by the wavelet technique (blue circles) and EC technique (orange squares); The tall-tower LE is calculated by the EC technique.*

To further evaluate the airborne wavelet LEs, the flight-level wavelet LEs and EC LEs at 100m and the EC LEs of tall-tower US-PFa at 122m are compared (Figure 3b). The comparison of LE is only in July because the tall towers measured inaccurate negative EC LEs at 122 m height during the August IOP, while EC LEs at 30 m and 396 m were positive. The EC LEs in August and September have been excluded from the quality control process. The airborne wavelet-calculated LEs compare reasonably well with the airborne EC LEs at 100 m height and the one-hour averaged US PFa LEs at 122 m height. However, the flight-level wavelet LEs do not match the EC LEs at the flight level and US PFa tower height. The difference between airborne wavelet LEs and airborne EC LEs may be due to the fact that wavelet LEs only consider the scales from 8 m to 8 km. The US PFa LEs are one-hour averaged EC LEs. The one-hour mean EC LEs account for a footprint of 10-23 km, given the 2.9-6.4 m s^{-1} averaged wind speeds (Table 1), while the airborne wavelet-calculated LE represents about 23-30 km spatial distance in 5 minutes. The tower measurements at a fixed point only represent a small area around the flux tower in the footprint flux map (Figure 12 in Butterworth et al., 2021). As a result, the reason for the different LEs obtained by the tower and airborne measurements could be that the aircraft measured landscape-level LEs generated by local surface heterogeneities and mesoscale forcings in 30 x 30 km^{-2} extended domains.

3. Results

3.1 Surface Flux Variability Measured by Flux Towers

Seventeen ISFS flux towers provide continuous spatial flux records in the CHEESEHEAD19 domain throughout the campaign from July to September (Locations in Figure 1). Surface heterogeneity influences the surface energy balance and resulting atmospheric responses in LE variations. The full-monthly mean (30/31 days averaged value) *Rnet*, ground heat flux (*Gsfc*), and LE are calculated between 1300 and 0000 UTC to provide daytime fluxes in July, August, and September, since the latest sunrise and earliest sunset time were 1252 and 0044 UTC on 28 September, respectively (all sunrise and sunset time shown in Table 1). The spatial incoming available energy (*Rnet*+ *Gsfc*) varied from 425 Wm^{-2} to 290 Wm^{-2} in July, from 350 Wm^{-2} to 270 Wm^{-2} in August, and from 230 Wm^{-2} to 130 Wm^{-2} in September in a 10 x 10 km^2 domain (Figure 4). The LE varied from 235 Wm^{-2} to 85 Wm^{-2} in July, from 190 Wm^{-2} to 95 Wm^{-2} in August, and from 120 Wm^{-2} to 20 Wm^{-2} in September. These spatial variabilities of fluxes in the 10 x 10 km^2 domain could come from the heterogeneous forested landscape, the topography of the surface, and atmospheric responses from surface forcing. This deployment strategy reveals the variation in surface and vegetation properties across the CHEESEHEAD19 domain. The tower-monthly mean of incoming available energy and LE decreased from July to September (the last column in Figure 4). The extended 3-month duration of the field experiment allows us to sample the seasonal shift in the surface energy budget partitioning as the study domain shifts from a LE-dominated late summer landscape to a greater sensible heat contribution early autumn landscape (Butterworth et al., 2021).

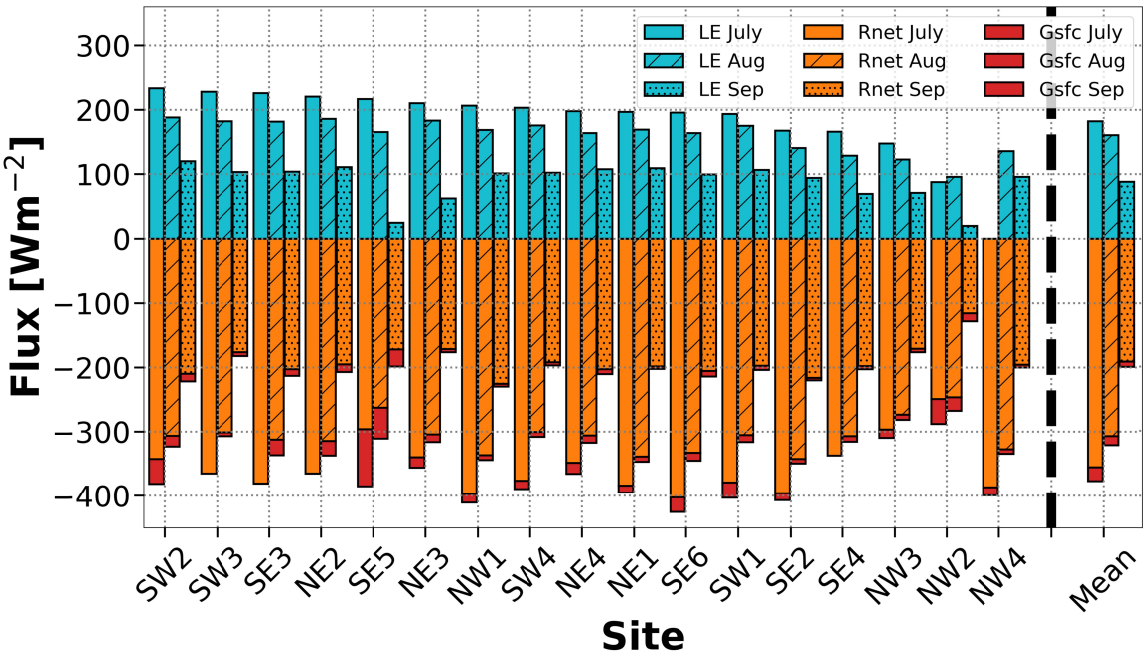

Figure 4. *The monthly-averaged daytime (1300 - 0000 UTC) LE, net radiation (Rnet), and ground heat flux (Gsfc) from the 17 EC towers and the 17-station mean values in July, August, and September. The sites are ordered with July LEs.*

3.2. LE variability

3.2.1 The temporal variability of leg-averaged LE

The leg-averaged LEs at the 100 m flight level reveal temporal variabilities. The leg-averaged LE is calculated by both wavelet (blue dots; by Equation S11) and EC (red squares; by Equation 2) techniques for every flight leg, on both morning and afternoon RFs (Figure 5). The wavelet LEs are generally in good agreement with EC LEs through time. The orange-shaded areas represent the standard deviations of the wavelet LEs within the leg indicating spatial variabilities. The RF-average LE ranged from 250 Wm^{-2} (12 July M and 22 August A), to 50 Wm^{-2} (20 August M and 28 September A) (Figure 5). These spatiotemporal variations reflect different surface types, wind conditions, and net radiation variations with time (Figure 1 and Table 1). The linear fit of leg-averaged LE indicates a decreasing trend from 210 to 80 Wm^{-2} from July to

September (Figure 5). In summary, the leg-averaged LE decreased from July to September, but the diurnal and synoptic variations of LEs cannot be ignored.

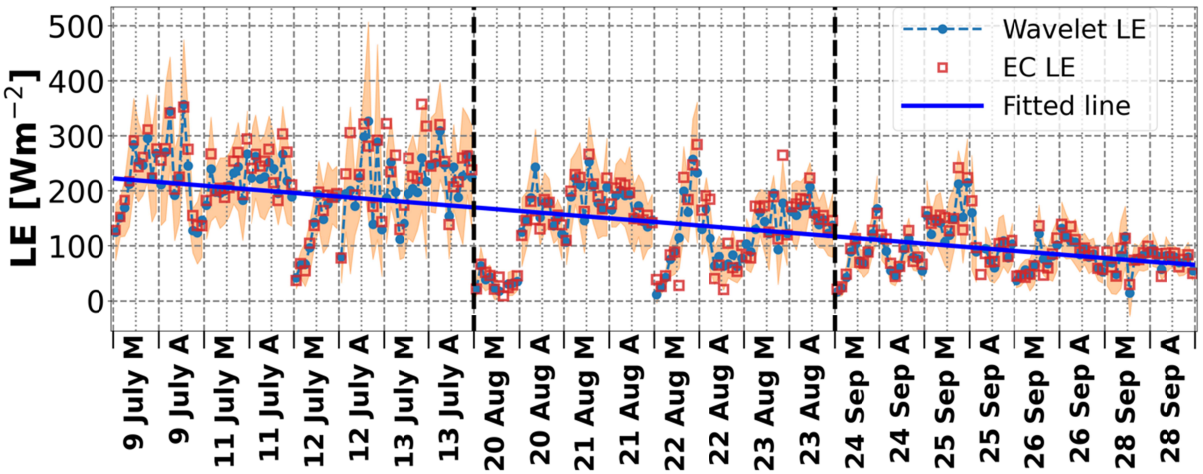

Figure 5*. The leg-averaged LE was calculated by wavelet technique (blue dots) with their standard deviation (orange shaded area) and EC technique (red squares) on legs. The fitted line shown as the blue line represents the trend of the leg-averaged LE in RFs from July to September.*

3.2.2 The Temporal Variability of Scale-resolved LE

The scale-resolved LE is calculated by Equation S11 for all flight legs to determine the scale contribution to the total LE over time and location. We examine all 12 days (Table 1), 4 from each IOP, each with a morning and an afternoon flight (Figure 6). The morning measurements include the first 10 flight legs, while the afternoon measurements consist of the last 10 flight legs in each day (Figure 6; separated by black dashed lines). The scale-resolved LE is averaged in each flight leg and is mostly between 62 m and 8 km as shown in Figure 6. The scale-resolved LE increases with time (leg number) as the total LE increases in the morning of 09 July, 12 July, 22 August, and 24 September, while it decreases in the afternoon of 09 July, 20 August, 22 August, and 26 September. However, these patterns are inconsistent for all dates, indicating the significant roles of PBL circulation and mesoscale advection in controlling local LEs other than radiation. The peak value of scale-resolved LE between 62 m to 8 km varies by as much as 10

Wm^{-2} on 12 July, 13 July, 20 August, and 22 August. The red-dashed lines represent the total LE. The daily temporal variation varies from 100 Wm^{-2} (28 September) to 280 Wm^{-2} (12 July). Although the total and scale-resolved LEs indicate strong temporal variation with legs, the primary scale is from 200 m to 4 km.

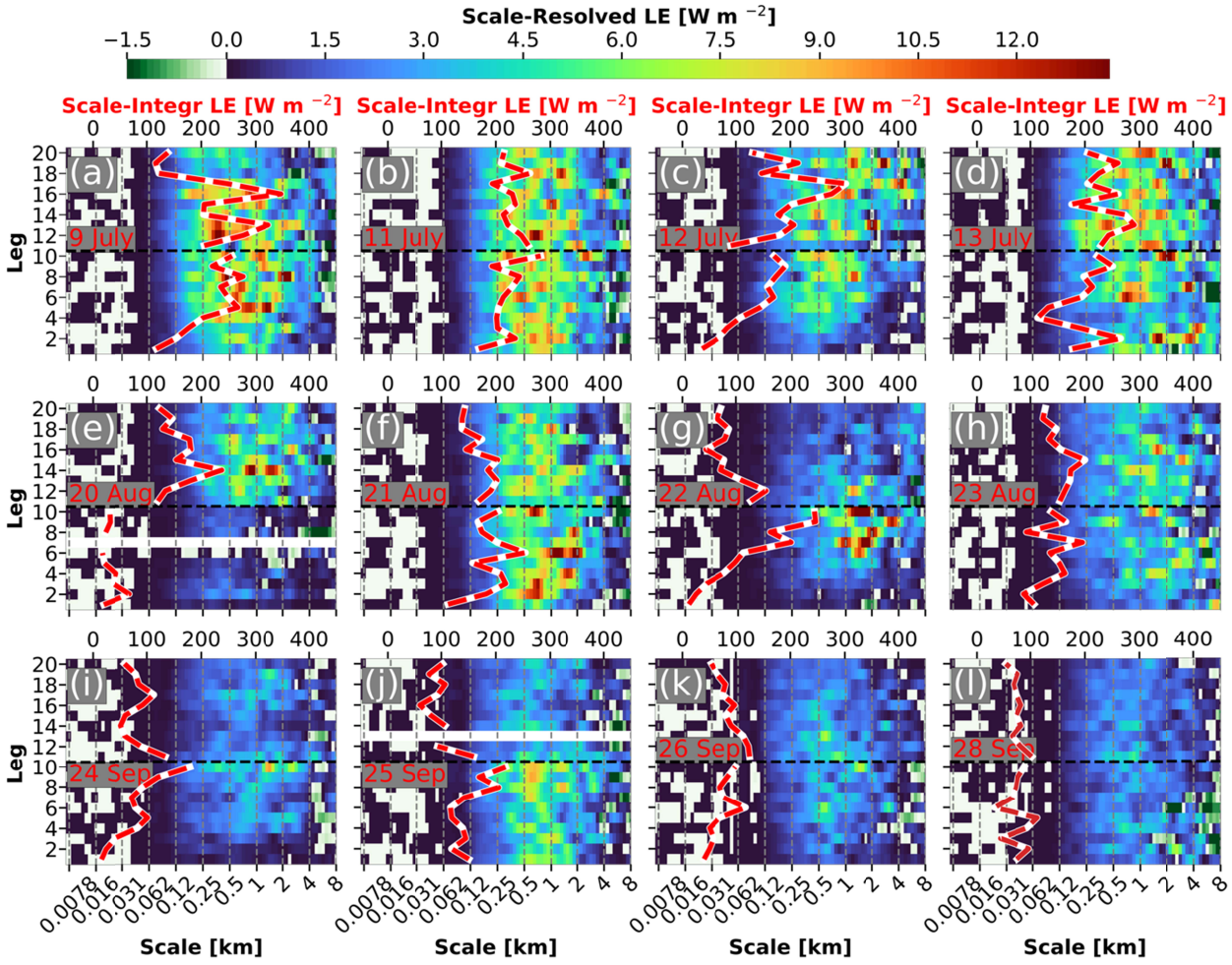

Figure 6*. The leg-averaged LE distributions on the scale (x-axis) and leg number (y-axis) for dates of (a) 9, (b) 11, (c) 12, and (d) 13 July; (e) 20, (f) 21, (g) 22, and (h) 23 August; (i) 24; (j) 25; (k) 26, and (l) 28 September. Legs 1-10 are for the morning, and Legs 11-20 are for the afternoon. The red-dashed lines represent the total LE (scale on upper x-axis).*

3.3 The Contributions of *w'* and r_v' on Scale-Resolved LE

3.3.1 Total LE Dependency

The scale-resolved LEs are composited at various total LEs ranging from 10-270 Wm^{-2} in 20 Wm^{-2} increments. The scale dependencies of LE, σ^2_w, and σ^2_{wv} from 7.8m to 8 km are depicted in Figures 7a-c. The distribution of scale-resolved LEs with values greater than 0.5 Wm^{-2} range from 200 m – 1.5 km to 100 m to 8 km, with the maximum scale-resolved LE increasing from 0.5 to 9 Wm^{-2} as the total LE linearly increases from 20 to 260 Wm^{-2} (white dashed contours in Figure 7a). Compared to the scale-resolved LE distributions, the scale-resolved σ^2_w with values greater than $5x10^{-3}$ m^2s^{-2} is in smaller scale ranges from 50m-700m to 16 m - 4 km. The scale-resolved σ^2_{wv} distribution with a value greater than $2\ x10^{-4}$ g^2kg^{-2} mainly focuses from 400 m - 8 km to 150 m - 8 km in scale as the total LE increases from 20 to 260 Wm^{-2}. As the total LE increases, the scale-resolved LE, $\sigma^2_{w,}$ and σ^2_{wv} distributions extend to broader ranges. For LE increases between 20 and 100 Wm^{-2}, the total σ^2_w (red dashed line in Figure 7b) quadruples (from 0.24 to 1.04 m^2s^{-2}), while the total σ^2_{wv} (red dashed line in Figure 7c) remains steady (around 0.02 g^2kg^{-2}). The total σ^2_w is nearly constant between 0.8 to 1.00 m^2s^{-2} as the total LE increases from 100 to 260 Wm^{-2}. However, the total σ^2_{wv} linearly increases from 0.018 to 0.048 g^2kg^{-2} from 100 to 220 Wm^{-2}. The characteristics of σ^2_w and σ^2_{wv} variations show the dominance of σ^2_w for low LE periods and the dominance of σ^2_{wv} for high LE periods.

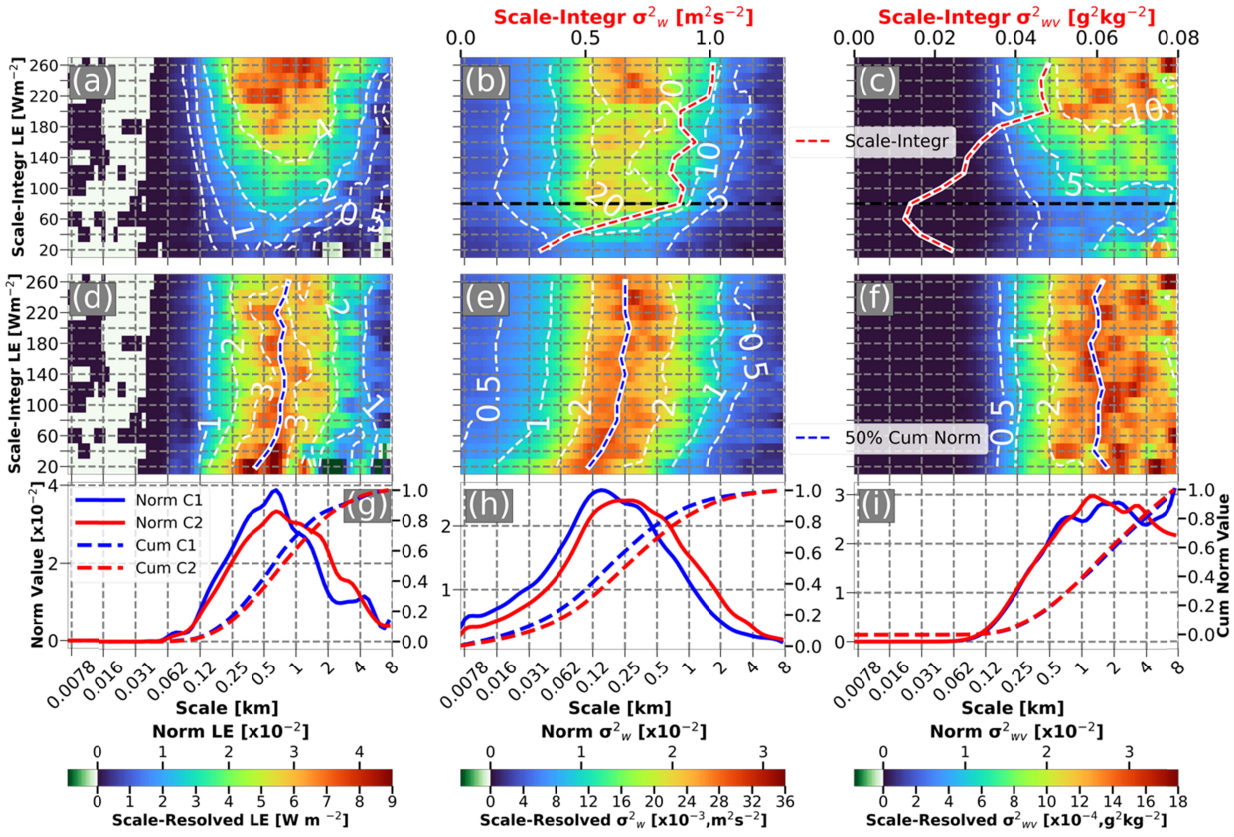

Figure 7. *The scale-dependent (a) LE, (b)* σ^2_w*, and (c)* σ^2_{wv}*, and normalized scale-dependent (d) LE, (e)* σ^2_w*, and (f)* σ^2_{wv} *distributions as a function of leg-integrated total LE from 20 to 260* Wm^{-2}*; The distributions of normalized scale-dependent and cumulative (g) LE, (h)* σ^2_w*, and (i)* σ^2_{wv} *for low-LE (from 20 to 80* Wm^{-2}*) legs, referred to as C1, and for high-LE (from 100 to 260* Wm^{-2}*) legs, referred to as C2. The white dashed contours in (a)-(f) represent the normalized values (see color bar below). The red-dashed lines in (a)-(c) represent the leg-averaged scale-integrated values; the blue dashed lines in (d)-(f) represent the scale of the median LE scale (50% cumulative values).*

It is difficult to investigate the relative scale contributions of σ^2_w, and σ^2_{wv} to LE due to their value and scale-range variations as the total LE increases in Figure 7a-c. To address this issue, the scale-resolved LE, σ^2_w, and σ^2_{wv} are normalized based on Equations S10 and S12. The 50 % value in the cumulative normalized scale-resolved LE, σ^2_w, and σ^2_{wv} are marked as blue dashed lines (Figure 7d-f). The distribution of normalized scale-resolved LE with values greater than 1% shifts from 120 m – 1.5 km to 250 m – 2 km as the total LE increases from 20 to 260 Wm^{-2}

(Figure 7d). In the meantime, the normalized scale-resolved σ^2_w with values greater than 1% range shifting from 16 m – 800m to 50 m to 2 km, and the normalized scale-resolved σ^2_{wv} with values greater than 0.5% ranges from 150 m to 8 km as the total LE increases. The 50% cumulative normalized scale-resolved LE is located in scale from 420 m to 700 m as total LE increases from 20 to 80 Wm^{-2} and then maintains its scales at ~700 m from 100 – 260 Wm^{-2}. The 50% cumulative normalized scale-resolved σ^2_w also has an increasing trend in the scale from 120 m to 250 m as total LE from 20 to 120 Wm^{-2} and then maintains its location around 250 m as total LE increases to 260 Wm^{-2}. The scale of 50% cumulative normalized scale-resolved σ^2_{wv} is located around 1.2 -1.7 km without an increasing trend.

Based on normalized and cumulative values, the scale-resolved LEs are divided into two categories. The first category (C1) contains low total LE 100 m AGL flight legs (between 20 and 80 Wm^{-2}), while the second category (C2) contains high total LE values (between 100 and 260 Wm^{-2}), as shown in Figures 7g-i. The normalized scale-resolved LE in C1 is larger than that in C2 in scales ranging from 250 m to 800 m, while normalized scale-resolved LE in C2 is larger than that in C1 in scales ranging from 800 m to 4 km. The same pattern is observed in the distribution of normalized scale-resolved σ^2_w, but with the separation scale at 250 m (Figures 7g and 7h). The distribution of normalized scale-resolved LE and σ^2_w are different for the two categories. However, the normalized scale-resolved σ^2_{wv} has the same values from 8 m to 800 m in C1 and C2. The cumulative normalized values show the percentage of resolved scales in LE, σ^2_w, and σ^2_{wv}.

Operational numerical weather prediction (NWP) systems can use scale-resolved normalized and cumulative values to guide sub-grid scale parameterization. The highest resolution operational non-hydrostatic NWP systems approach horizontal grid spacings of 1.0 km, e.g. the Application of Research to Operations at Mesoscale (AROME) runs at 1.2 km, and the Consortium for Small-scale Modeling (COSMO) runs at 1.1 km in parts of Europe (e.g., Benjamin et al. (2019); Dowell et al. (2022)). In general, the effective model resolution is coarser than the grid spacings. If we assume that 6 grid points are needed to adequately resolve a wavelike phenomenon (Benjamin et al. 2019), the smallest resolvable feature in a 1 km grid model is 6 km (e.g., Chapter 11 in Lackmann 2011). The spectral distribution in Figure 7 indicates that the

unresolvable normalized percentages are 87-89% in LE, 95-97% in σ^2_w, and 66-68% in σ^2_{wv} for the highest resolvable resolution of 6 km in the highest-resolution NWP systems currently in operation. The high unresolvable normalized percentages indicate LE and σ^2_w are dominated more by the forcings on smaller scales, compared to that in σ^2_{wv}. Thus, the unresolvable scale-dependent values driven by scales smaller than NWP resolution must be carefully parameterized in the NWP systems.

3.3.2 Temporal dependency

To investigate the temporal variability of scale-resolved LE, $\sigma^2_{w,}$ and σ^2_{wv}, the LE is composited on 20 flight legs from morning to afternoon in flight IOPs of July, August, and September (Figures 8a-c). Even though the first flight took off at different times and the sunrise and sunset times varied in RFs of IOPs from July to September (Table 1), the same legs from all four RFs in the morning and in the afternoon in each IOP are averaged. The distribution of scale-resolved LE with values greater than 2 Wm^{-2} is shrunk from 120 m - 4 km in July to 250 m - 2 km in September, showing flight-leg dependent temporal variability in each month (Figure 8a). Similarly, the distribution of scale-resolved σ^2_{wv} with values greater than 10^{-4} g^2kg^{-2} shrunk ranging from 120 m -8 km in July to 250m - 4km in September (Figure 8c). However, the distribution of scale-resolved σ^2_w differs from that in scale-resolved LE and σ^2_{wv}, with values greater than 0.5 x 10^{-3} m^2s^{-2} observed in 32 m – 4 km in August, but shifts to 10 m – 3 km in July and September.

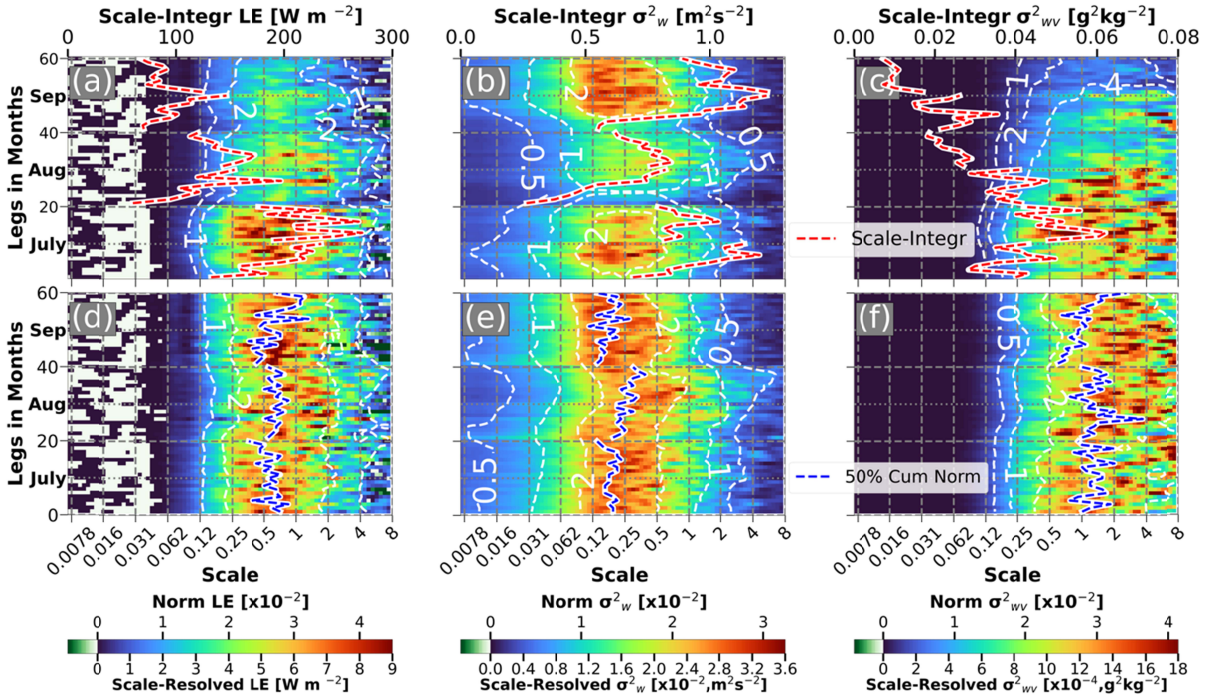

Figure 8. As in Figure 7 (a)-(f), but as a function of *leg numbers (y-axis) averaged monthly IOPs in July, August, and September.*

To investigate the relative scale distributions of LE, σ^2_w, and σ^2_{wv}, the normalized scale-resolved LE, σ^2_w, and σ^2_{wv} are calculated based on legs in IOPs. The range of normalized scale-resolved LEs is from 120 m to 4 km for values greater than 1% of the cumulative normalized LE, and for values greater than 2% range from 200 m to 2 km (Figure 8d). In August, the scale range of normalized scale-resolved LE with values greater than 1% shifted from 120 m – 4 km in July and September to 160 m – 6 km. The temporal variation is shown as the scale of 50% of cumulative normalized scale-resolved LE (blue dashed lines in Figure 8d-f). The scale of 50% of cumulative normalized scale-resolved LE ranges from 350 m to 700 m in July, 500 m – 840 m in August, and 350 m to 1.2 km in September. In the meantime, the normalized scale-resolved σ^2_w distribution is mainly located between 32 m and 2 km (Figure 8e). The distribution of normalized scale-resolved σ^2_w with values greater than 1% among IOPs has a similar scale distribution to the normalized scale-resolved LE with a larger scale range in August than that in July and September. The scale of 50% of cumulative normalized scale-resolved σ^2_w varies from 130 m to 210 m in July, 200 m – 350 m in August, and 100 m to 270 m in September. The normalized scale-resolved σ^2_{wv} with a value greater than 1% ranges between 200 m and 8 km (Figure 8f).

The scale of 50% of cumulative normalized scale-resolved σ^2_{wv} varies from 1 km to 2 km in July, 700 m – 3.6 km in August, and 600 m to 2.6 km in September. Even though strong temporal variations exist in flight legs and in IOPs, the mean scale of 50% of the cumulative normalized scale-resolved value is 640 m of LE, 200 m of σ^2_w, and 1.25 m of σ^2_{wv}, respectively. The primary contribution to scale-resolved LE should be in the overlap scales between σ^2_w (32 m – 2 km) and σ^2_{wv} (200 m – 8 km) ranging between 200 m and 2 km, which coincides with the primary scale-resolved LE distribution with values greater than 2% ranging from 200 m to 2 km. Despite the different scale distribution between σ^2_w and σ^2_{wv}, the primary scale contribution between 200 m and 2 km from σ^2_w and σ^2_{wv} to LE indicates large eddies in the PBL primary sources of vertical moisture transport.

3.4 The Contributions of Turbulent, Large, and Mesoscale Eddies on LE

3.4.1 Total LE Dependency

To better understand the scale-dependent impacts of w' and r_v' to LE, the scales from 8m to 8 km are classified into three ranges. Previous studies (e.g., Mauder et al., 2007; Paleri et al., 2022) used a 2 km threshold to divide the scales into the turbulent scale in PBL and mesoscale to investigate mesoscale contributions to the total LE. Our analysis of scale-resolved σ^2_w shows that the primary scale-resolved σ^2_w occurs within a wavelength of 2 km (Figure 7e and Figure 8e), which aligns with the PBL depth. Orlanski (1975) used a threshold scale of 200 m to differentiate between turbulence (micro β scale < 200m) and organized eddies (micro α scale > 200 m). Our analysis of scale-resolved σ^2_{wv} shows that the 200 m marks the beginning of the σ^2_{wv} scale contributing to LE. Thus, the scales are divided into three ranges: 8 m - 200m (turbulent scale in PBL), 200 m – 2 km (large-eddy scale in PBL), and 2 km – 8 km (mesoscale) to explore their contributions to σ^2_w, $\sigma^2_{wv,}$ and LE under different total LE values and IOP legs. Note that both the turbulent and large-eddy scales fall in the inertial subrange for isotropic turbulence in the surface layer (Stull 1988).

610 The scale-resolved LE in the three scale ranges increases as the total LE increases from 20 to 260
611 Wm^{-2}, but the percentage contributions to total LE among the three scale ranges only slightly
612 change (Figure 9a). The large-eddy scale contributes to the highest percentage of total LE,
613 ranging from 69 to 75 % (the orange dashed line in Figure 9a). The mesoscale contributes to the
614 second largest percentage of total LE, ranging from 9% to 23 % (the blue dashed line). The
615 turbulent-scale eddy only contributes 8 -15 % of the total LE (the red dashed line). The majority
616 of the σ^2_w is found in turbulent and large eddy scales, accounting for over 90% of the total σ^2_w.
617 As the total LE increases from 20 to 260 W m^{-2}, the turbulent σ^2_w decreases from 65% to 42%,
618 while the σ^2_w in the large-eddy scale increases from 31% to 51%. The mesoscale σ_w only
619 contributes 3% -9% of the total σ^2_w. On the other hand, the σ^2_{wv} is mainly found in the large-
620 eddy scale and mesoscale, accounting for over 96% of total σ^2_{wv}, while the turbulent scale σ^2_{wv} is
621 only 3-4% of total σ^2_{wv}, which could be biased by the temporal response of the water vapor
622 sensor.
623
624 To examine the scale contribution from the covariance of w' and r_v' to the LE, $cov_{(w,wv)}$ in the
625 three scale ranges is calculated based on Equation S13 (dotted lines in Figure 9a). The largest
626 difference between $cov_{(w,wv)}$ and LE is observed in the large-eddy scale, accounting for 7.2%
627 mean percentage of total LE. The mean difference in turbulent scale and mesoscale is 2.9% and
628 4.3% of total LE, respectively. The most significant difference is observed in the total LE
629 between 20 and 60 Wm^{-2}, particularly the difference is 15% in the mesoscale as the total LE
630 ranges from 20 to 40 Wm^{-2}. Overall, the analysis of $cov_{(w,wv)}$ revealed similar results to the
631 directly calculated LE, with the majority of LE (58-68%) found in the large-eddy scale, followed
632 by the mesoscale (21-25%), and the smallest percentage (8-15%) of the total LE found in the
633 turbulent scale.
634

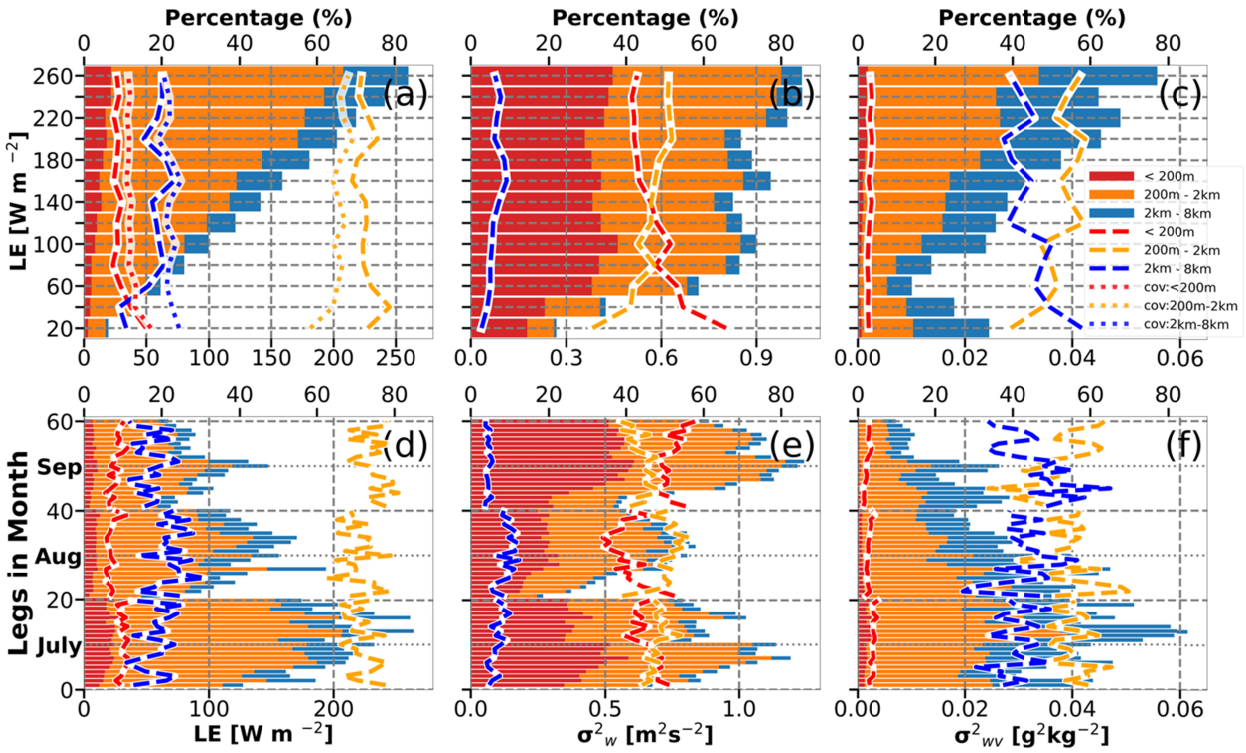

Figure 9. *The partitions of turbulent scale (red), large eddy scale (orange), and mesoscale (blue) contributions based on leg-integrated LE in LE (a and d),* σ^2_w *(b and e) and* σ^2_{wv} *(c and f) sorted with LE from 20 -260* Wm^{-2} *(a-c) and leg time (d-f). The red-, orange-, and blue-dashed lines represent the leg-averaged scale-integrated contributions (expressed as percentages) from turbulent scale, large-eddy scale, and mesoscale respectively. The dotted lines in (a) are the corresponding* $cov_{(w,wv)}$ *averages in the three scale ranges.*

3.4.2 Temporal dependency

The contributions in different scale ranges to monthly IOP-mean total LEs are similar to the previous analysis, but temporal variations exist in legs and in IOPs (Table 3 and Figures 9d-f). The turbulent scale contributions in LE vary from 10.2 % to 7.0 % from July to September. The large-eddy scale contributions in LE vary from 70.4% to 74.7 % from August to September. The mesoscale contributions vary from 22.6% to 17.0% from August to September. In monthly IOP-mean σ^2_w variations, the turbulent scale contributions vary from 40.5% to 51.6%. The large-eddy scale contributions vary from 50.3% to 43.9%, and the mesoscale contributions vary from 9.2% to 4.4 %. In the monthly IOP-mean σ^2_{wv} variation, the turbulent scale contributions vary from 4.0%

to 2.3 %. The large-eddy scale contributions vary from 55.2 % to 51.8 %, and the mesoscale contributions vary from 40.8% to 45.9%. The monthly IOP-mean variations range from 3.2 % to 5.6% in LE, from 6.4 % to 11.1% in σ^2_w, and 1.7% to 5.1% in σ^2_{wv} in the three scale ranges.

Table 2: *The monthly leg-averaged mean and the standard deviation in LE, σ^2_w, and σ^2_{wv} in three spatial ranges (turbulent scale, large-eddy scale, and mesoscale), expressed as a percentage of the total.*

Variable		July		Aug		Sep	
		Mean	Std	Mean	Std	Mean	Std
LE	Turb (%)	10.2	1.3	7.0	1.2	8.3	1.5
	Large-eddy (%)	71.3	3.8	70.4	4.4	74.7	3.9
	Meso (%)	18.4	4.3	22.6	4.4	17.0	4.0
σ^2_w	Turb (%)	45.5	3.0	40.5	4.7	51.6	2.9
	Large-eddy (%)	47.7	2.2	50.3	3.7	43.9	2.8
	Meso (%)	6.8	1.6	9.2	2.1	4.4	0.6
σ^2_{wv}	Turb (%)	4.0	0.6	2.8	0.6	2.3	0.7
	Large-eddy (%)	55.2	4.8	54.6	6.9	51.8	7.8
	Meso (%)	40.8	5.0	42.6	7.1	45.9	8.3

The temporal variations in legs are represented by standard deviations. The major temporal variations in legs are in the largest and second-largest scale ranges of LE (the large-eddy scale and mesoscale), σ^2_w (the turbulent and large-eddy scales), and σ^2_{wv} (the large-eddy scale and mesoscale) shown in Figures 9d-f. The temporal LE variations in the large-eddy scale and mesoscale LE have standard deviations of 3.8% – 4.3%. The temporal σ^2_w variations in turbulent and large-eddy scales range from 2.2 % to 4.7%. The temporal σ^2_{wv} variations in the large-eddy scale and mesoscale range between 4.8% and 7.8%. The smallest temporal variations in legs are 1.2%-1.5% in turbulent LE, 0.6%-2.1% in mesoscale σ^2_w, and 0.6%-0.7% in turbulent σ^2_{wv}.

673 **3.5 Forcing scales of w' and rv': Implications and Additional Evidence**
674
675 Results above indicated that the scale forcings are different in σ^2_w, and σ^2_{wv} to LE. The primary
676 scale forcings are the large-eddy scale and mesoscale in LE, the turbulent scale and large-eddy
677 scale in σ^2_w, and the large-eddy scale and mesoscale in σ^2_{wv}. Couvreux et al. (2005) and
678 Couvreux et al. (2006) investigated r_v variability in the convective boundary layer (CBL) with
679 airborne measurements and large eddy simulations (LES) and also found that the characteristic
680 length scale of r_v is larger than w. Both observations and LES indicate the intrusions of dry free-
681 troposphere air into the growing CBL. These intrusions generally lack negative buoyancy but
682 they may interact with large-eddy circulations that transport the drier free-troposphere into the
683 lower CBL, and occasionally even close to the surface. Moreover, Couvreux et al. (2005) and
684 Couvreux et al. (2006) found that large amounts of dry air that are quickly incorporated into the
685 CBL prevent full homogenization by turbulent mixing. Near the heated land surface, these dry
686 air intrusions may become negatively buoyant. In our study, the flight tracks at 400 m AGL with
687 CRL measurements provide 2D vertical profiles of r_v to investigate the vertical r_v distribution and
688 transport process (Figure 10). For instance, the 400 m AGL flight in situ data measured
689 downward transport (negative flight-level w) of relatively drier air (~9.2 g kg^{-1}) at the distance of
690 11.5 km, 17 km, and 18.5 km (Figure 10a). The CRL sampled these three drier air parcels and
691 shows that they penetrated toward the 100 m AGL (Figure 10b). The horizontal scales of dry and
692 moist air parcels (PBL large eddies) sampled by CRL are a few kilometers, which is consistent
693 with the return flight-level σ^2_{wv} scaling from 200 m – 8 km at 100 m AGL in Figure 2i,
694 indicating large-eddy and mesoscale forcings in r_v. Since the time difference between the two
695 flight legs is 5- 10 minutes, and the chosen RFs that are closest perpendicular to the prevailing
696 wind, the r_v at 100 m AGL between CRL and flight level data do not correspond very well.
697 However, r_v shows a shift of dry air (~9 g kg^{-1}) from 12.5 km for the CRL measurement to 13.5
698 km for the airborne in situ measurement at around 100 AGL. Although lacking 2D w' profiles
699 from the airborne measurements, variability in w' at smaller scales than r_v' is observed at 400 m
700 AGL (Figure 10a). Moreover, w' at the 100 m return flight shows small-scale variability between
701 16 m and 1.5 km (Figure 2h) indicating the dominant turbulent and large-eddy scale forcings.
702

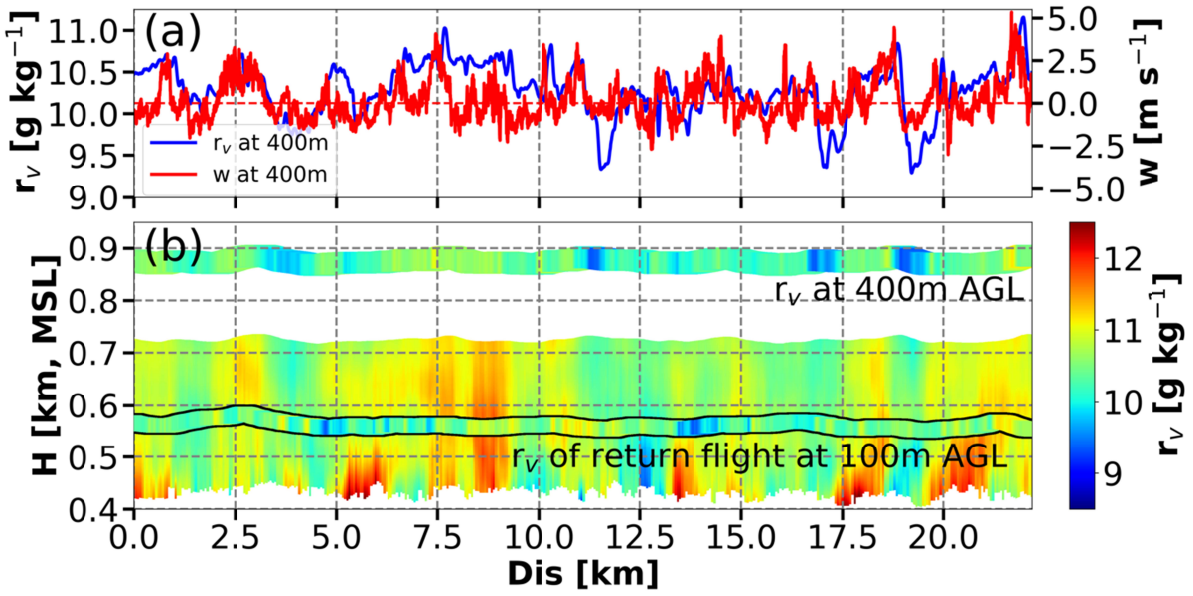

Figure 10. *(a) Flight-level r_v (blue line) and w (red line) for RF03 leg 2 at 400 m. (b) Flight-level in situ r_v and CRL 2D profile of r_v. Since the surface height varies along the flight track, the 2D r_v profile uses mean sea level (MSL) as the height reference. The colored return flight at 100 m AGL is the r_v along the flight leg in Figure 2, where the flight track is the same as this flight, but at a different height.*

4. Discussion

The leg-averaged and scale-resolved LE show seasonal variations from July to September. The leg-averaged LE was up to 250 Wm^{-2} in a single 3-hour RF, and the leg-averaged LE decreased from July to September. The scale-resolved LE in RFs mainly distributes between 62 m and 8 km with scale-resolved temporal variability. However, the general diurnal patterns of leg-averaged LE didn't occur for all IOP days highlighting the significant roles of PBL circulation and mesoscale advection in controlling local LEs other than radiation. These temporal variations are related to the combination of differences in surface types, wind conditions, and net radiation as the aircraft samples in space and time and require rectification and footprint-identification approaches for any mapping of LE using airborne data (Metzger et al., 2013; Sun et al., 2023).

The primary transport process in the PBL is turbulent-driven fluxes, which can be directly measured by the EC technique. The mesoscale forcing is not adequately resolved by traditional EC measurement due to short averaging times, surface heterogeneity, PBL circulation, and lack of closure in the energy budget (Mauder et al., 2006; Sun et al., 2006; Mahrt, 2010; Foken et al., 2011; Charuchittipan et al., 2014; Butterworth et al., 2021). Hence the expected value from a single-tower measurement tends to systematically underestimate the surface heat flux. Compared to shortcomings in conventional EC measurements, large eddy simulation (LES) studies can advance the understanding of scale-dependent physical processes in fluxes that EC tower measurements cannot resolve. Margairaz et al. (2020) investigated organized PBL circulations over the heterogeneous surface over a broad range of atmospheric stability conditions in LES. Couvreux et al. (2005) used airborne measurements and LES to investigate r_v variability in PBL at the large-eddy scale and sub-mesoscale (a few kilometers) in the convective boundary layer (CBL). The vertical transport associated with the large eddy to mesoscale circulations could be missed by single tower-based measurements, and it can be overestimated if the tower happens to be located near mesoscale boundaries (Mahrt, 2010; Charuchittipan et al., 2014; Helbig et al., 2021).

The wavelet technique applied to high-frequency airborne data allows us to analyze atmospheric flux contributions from the turbulent scale to the mesoscale above heterogeneous terrain during

741 the CHEESEHEAD19 field campaign. The covariance of *w'* and r_v*'* impacts the LE at different
742 scales with temporal variability. The scale distribution of LE, σ^2_w, and σ^2_{wv} are different, with the
743 dominant scales ranging from 120 m to 4 km for LE, from 32 m to 2 km for σ^2_w, and from 200 m
744 to 8 km for σ^2_{wv}. The primary contribution to scale-resolved LE should be in the overlap scales
745 between σ^2_w and σ^2_{wv} ranging between 200 m and 2 km, which coincides with the primary scale-
746 resolved LE distribution. The temporal variation is shown as the scale of 50% of cumulative
747 normalized scale-resolved values. In these terms, the 50% scale (or median scale) ranges from
748 350 m to 1.2 km (3-IOP mean: 640 m) for LE, from 130 m to 200 m – 350 m (mean: 200 m) for
749 σ^2_w, and from 600 m to 3.6 km (mean: 1250 m) for σ^2_{wv}. The different scale distributions of LE,
750 σ^2_w, and σ^2_{wv} suggest that large eddies in the 200 m - 2 km width range are the primary sources
751 of vertical moisture transport across the PBL, despite different scale contributions of σ^2_w and
752 σ^2_{wv}.
753
754 We defined the turbulent, large-eddy, and mesoscale as 8 m - 200 m, 200 m – 2 km, and 2 - 8 km
755 respectively. 85-92 % of total LE falls in large-eddy scale and mesoscale, 90% of the total σ^2_w
756 falls in turbulent scale and large-eddy scale, and 96% of the total σ^2_{wv} falls in large-eddy scale
757 and mesoscale. Most variance in LE, σ^2_w, and σ^2_{wv} is found in the large-eddy scale, with 69-75 %
758 of total LE, 31-51% of the total σ_w, and 39-59 % of the total σ^2_{wv}. The temporal monthly IOP-
759 mean variations range from 1.7% to 11.1% of total values. The temporal variations in legs are
760 represented by standard deviations ranging from 0.6% -7.8% of total values. Although diurnal
761 and seasonal LE variation exists, this finding implies the dominance of the large eddy scale for
762 LE, driven by a combination of *w'* and r_v 'variations.
763
764 This large-eddy scale in PBL is not captured even by the finest-resolution operational regional
765 non-hydrostatic NWP systems currently in operation, with horizontal grid spacings near 1 km
766 (Dowell et al., 2022). The unresolved cumulative normalized percentages within scales less than
767 6 km (the minimum size of a feature resolved by a 1 km grid) are 99% in LE, 99% in σ^2_w, and
768 94-96% in σ^2_{wv}. These high percentages of unresolvable scale-dependent values driven by scales
769 smaller than NWP resolution explain the continued need for PBL parameterizations in NWP
770 models.

This observational study describes the spatiotemporal LE variation and the impacts of w and r_v during the CHEESEHEAD19 field campaign. The large-eddy transport process contributes most of the total LE across the daytime PBL in the summer of northern Wisconsin. This analysis complements published LE variations on scales, which primarily present scale-dependent LE analysis and lack detailed scale-dependent vertical velocity and water vapor contributing information to LE.

The dominant scales of LE, w, and r_v are height-dependent, as evident from airborne measurements and LES simulations (Couvreux et al., 2005). The w and r_v in PBL are determined by not only surface evapotranspiration, but entrainment from the free atmosphere, PBL circulation and depth, and mesoscale advection (Linné et al., 2006). Future studies should further explore the height-dependent scale-resolved LE and the impacts of w and r_v on LE by applying the wavelet technique to airborne in situ data collected at multiple flight levels, or, better, by combining full profiles of airborne Raman lidar r_v data with Doppler lidar w measurements.

5. Conclusions

This study uses airborne measurements collected during the CHEESEHEAD19 field experiment to quantify the multi-scale diurnal and seasonal variation of latent heat flux (LE) and of its components (w and r_v) over a heterogeneous surface in northern Wisconsin from July to September 2019. Wavelet analysis of high-frequency measurements along the 25-30 km airborne tracks is used to evaluate characteristic scales of LE and its components, w and r_v , in the range of 8 m to 8 km. All data were collected during the daytime, under fair-weather conditions, at 100 m AGL, or roughly 3-4 times the tree canopy height. The two main conclusions are as follows:

- The dominant scale is rather short for w (32 m – 2 km), longer for r_v (200 m to 8 km), and intermediate for LE (120 m to 4 km), which depends on the covariance of w and r_v.
- Most variance in LE, σ^2_w, and σ^2_{wv} is found in the large-eddy scale, which we define as between 0.2 – 2.0 km, with σ^2_w containing substantial variability also in the turbulent scale (8 m – 200 m in this study) and σ^2_{wv} in the mesoscale (2-8 km in this study).

Clearly, the PBL will need to be parameterized in NWP models in the foreseeable future. Further studies should compare the different atmospheric fluxes between the airborne measurements and model simulation to improve the parameterization of PBL fluxes (Hu et al., 2023).

Acknowledgments. This study was funded and supported by the National Science Foundation (NSF) Grants AGS-1917693 and AGS-1917701, by the Department of Energy (DOE) Atmospheric System Research (ASR) Grant SC0020171, and by the National Aeronautics and Space Administration (NASA) 80NSSC20K0663, with additional support for scientific airborne data collection activities from the University of Wyoming King Air team. The CHEESEHEAD19 field campaign was supported by NSF Grant AGS-1822420. US-PFa observations were supported by a subaward to Desai from the DOE Ameriflux Network Management Project. The CHEESEHEAD19 data are provided by NSF-funded NCAR/EOL via the respective projects' Field Catalogs. The present study benefitted from the hard work of the many additional CHEESEHEAD19 participants to collect the data that helped enable this study.

Data availability statement. The UWKA in situ data and surface-based flux tower data are available on the EOL CHEESEHEAD website (https://www.eol.ucar.edu/field_projects/cheesehead). The land cover classification of NLCD 2019 can be found on the Multi-Resolution Land Characteristics Consortium (MRLC) website (https://www.mrlc.gov/data/nlcd-2019-land-cover-conus).

References

Attié, J.-L., & Durand, P. (2003), Conditional Wavelet Technique Applied to Aircraft Data Measured in the Thermal Internal Boundary Layer During Sea-Breeze Events. *Boundary-Layer Meteorology, 106*(3), 359-382. https://doi.org/10.1023/a:1021262406408.

Aubinet, M., Vesala, T., & Papale, D. (2012), Eddy covariance: A practical guide to measurement and data analysis. https://doi.org/10.1007/978-94-007-2351-1.

Avissar, R., & Schmidt, T. (1998), An Evaluation of the Scale at which Ground-Surface Heat Flux Patchiness Affects the Convective Boundary Layer Using Large-Eddy Simulations. *Journal of the Atmospheric Sciences, 55*(16), 2666-2689. https://doi.org/10.1175/1520-0469(1998)055<2666:Aeotsa>2.0.Co;2.

Bange, J., Beyrich, F., & Engelbart, D. A. M. (2002), Airborne measurements of turbulent fluxes during LITFASS-98: Comparison with ground measurements and remote sensing in a case study. *Theoretical and Applied Climatology, 73*(1), 35-51. https://doi.org/10.1007/s00704-002-0692-6.

Benjamin, S. G., Brown, J. M., Brunet, G., Lynch, P., Saito, K., & Schlatter, T. W. (2019), 100 Years of Progress in Forecasting and NWP Applications. *Meteorological Monographs, 59*, 13.11-13.67. https://doi.org/10.1175/amsmonographs-d-18-0020.1.

Berger, B. W., Davis, K. J., Yi, C., Bakwin, P. S., & Zhao, C. L. (2001), Long-Term Carbon Dioxide Fluxes from a Very Tall Tower in a Northern Forest: Flux Measurement Methodology. *Journal of Atmospheric and Oceanic Technology, 18*(4), 529-542. https://doi.org/10.1175/1520-0426(2001)018<0529:Ltcdff>2.0.Co;2.

Beyrich, F., Herzog, H. J., & Neisser, J. (2002), The LITFASS project of DWD and the LITFASS-98 experiment: The project strategy and the experimental setup. *Theoretical and Applied Climatology, 73*(1-2), 3-18. https://doi.org/10.1007/s00704-002-0690-8.

Beyrich, F., & Mengelkamp, H.-T. (2006), Evaporation over a Heterogeneous Land Surface: EVA_GRIPS and the LITFASS-2003 Experiment—An Overview. *Boundary-Layer Meteorology, 121*(1), 5-32. https://doi.org/10.1007/s10546-006-9079-z.

Bou-Zeid, E., Anderson, W., Katul, G. G., & Mahrt, L. (2020), The Persistent Challenge of Surface Heterogeneity in Boundary-Layer Meteorology: A Review. *Boundary-Layer Meteorology, 177*(2-3), 227-245. https://doi.org/10.1007/s10546-020-00551-8.

Butterbach-Bahl, K., Kögel-Knabner, I., & Han, X. (2011), Steppe ecosystems and climate and land-use changes—vulnerability, feedbacks and possibilities for adaptation. *Plant and Soil, 340*(1-2), 1-6. https://doi.org/10.1007/s11104-010-0651-4.

Butterworth, B. J., Desai, A. R., Townsend, P. A., Petty, G. W., Andresen, C. G., Bertram, T. H., et al. (2021), Connecting Land–Atmosphere Interactions to Surface Heterogeneity in CHEESEHEAD19. *Bulletin of the American Meteorological Society, 102*(2), E421-E445. https://doi.org/10.1175/bams-d-19-0346.1.

Charuchittipan, D., Babel, W., Mauder, M., Leps, J. P., & Foken, T. (2014), Extension of the Averaging Time in Eddy-Covariance Measurements and Its Effect on the Energy Balance Closure. *Boundary-Layer Meteorology, 152*(3), 303-327. https://doi.org/10.1007/s10546-014-9922-6.

Couvreux, F., Guichard, F., Masson, V., & Redelsperger, J. L. (2006), Negative water vapour skewness and dry tongues in the convective boundary layer: observations and large-eddy simulation budget analysis. *Boundary-Layer Meteorology, 123*(2), 269-294. https://doi.org/10.1007/s10546-006-9140-y.

Couvreux, F., Guichard, F., Redelsperger, J. L., Kiemle, C., Masson, V., Lafore, J. P., & Flamant, C. (2005), Water-vapour variability within a convective boundary-layer assessed by large-eddy simulations and IHOP_2002 observations. *Quarterly Journal of the Royal Meteorological Society, 131*(611), 2665-2693. https://doi.org/10.1256/qj.04.167.

Davis, K. J., Bakwin, P. S., Yi, C., Berger, B. W., Zhao, C., Teclaw, R. M., & Isebrands, J. G. (2003), The annual cycles of CO2 and H2O exchange over a northern mixed forest as observed from a very tall tower. *Global Change Biology, 9*(9), 1278-1293. https://doi.org/10.1046/j.1365-2486.2003.00672.x.

Desai, A. (2023). *AmeriFlux BASE US-PFa Park Falls/WLEF*. https://doi.org/https://doi.org/10.17190/AMF/1246090.

Desai, A. R., Bolstad, P. V., Cook, B. D., Davis, K. J., & Carey, E. V. (2005), Comparing net ecosystem exchange of carbon dioxide between an old-growth and mature forest in the upper Midwest, USA. *Agricultural and Forest Meteorology, 128*(1-2), 33-55. https://doi.org/10.1016/j.agrformet.2004.09.005.

Desai, A. R., Murphy, B. A., Wiesner, S., Thom, J., Butterworth, B. J., Koupaei-Abyazani, N., et al. (2022a), Drivers of Decadal Carbon Fluxes Across Temperate Ecosystems. *Journal of Geophysical Research: Biogeosciences, 127*(12). https://doi.org/10.1029/2022jg007014.

Desai, A. R., Paleri, S., Mineau, J., Kadum, H., Wanner, L., Mauder, M., et al. (2022b), Scaling Land-Atmosphere Interactions: Special or Fundamental? *Journal of Geophysical Research: Biogeosciences, 127*(10). https://doi.org/10.1029/2022jg007097.

Desjardins, R. L., MacPherson, J. I., Mahrt, L., Schuepp, P., Pattey, E., Neumann, H., et al. (1997), Scaling up flux measurements for the boreal forest using aircraft-tower combinations. *Journal of Geophysical Research: Atmospheres, 102*(D24), 29125-29133. https://doi.org/10.1029/97jd00278.

Desjardins, R. L., Macpherson, J. I., Neumann, H., Den Hartog, G., & Schuepp, P. H. (1995), Flux estimates of latent and sensible heat, carbon dioxide, and ozone using an aircraft-tower combination. *Atmospheric Environment, 29*(21), 3147-3158. https://doi.org/10.1016/1352-2310(95)00007-l.

Dewitz, J., & U.S. Geological Survey. (2021). *National Land Cover Database (NLCD) 2019 Products*. https://doi.org/doi:10.5066/P9KZCM54.

Dowell, D. C., Alexander, C. R., James, E. P., Weygandt, S. S., Benjamin, S. G., Manikin, G. S., et al. (2022), The High-Resolution Rapid Refresh (HRRR): An Hourly Updating Convection-Allowing Forecast Model. Part I: Motivation and System Description. *Weather and Forecasting, 37*(8), 1371-1395. https://doi.org/10.1175/Waf-D-21-0151.1.

Eder, F., Schmidt, M., Damian, T., Träumner, K., & Mauder, M. (2015), Mesoscale Eddies Affect Near-Surface Turbulent Exchange: Evidence from Lidar and Tower Measurements. *Journal of Applied Meteorology and Climatology, 54*(1), 189-206. https://doi.org/10.1175/jamc-d-14-0140.1.

Farge, M. (1992), Wavelet Transforms and Their Applications to Turbulence. *Annual Review of Fluid Mechanics, 24*, 395-457. https://doi.org/DOI 10.1146/annurev.fl.24.010192.002143.

Finnigan, J. J., Clement, R., Malhi, Y., Leuning, R., & Cleugh, H. A. (2003), A Re-Evaluation of Long-Term Flux Measurement Techniques Part I: Averaging and Coordinate Rotation. *Boundary-Layer Meteorology, 107*(1), 1-48. https://doi.org/10.1023/A:1021554900225.

Foken, T., Aubinet, M., Finnigan, J. J., Leclerc, M. Y., Mauder, M., & Paw U, K. T. (2011), Results Of A Panel Discussion About The Energy Balance Closure Correction For Trace

914 Gases. *Bulletin of the American Meteorological Society, 92*(4), ES13-ES18.
915 https://doi.org/10.1175/2011bams3130.1.
916 Foken, T., & Wichura, B. (1996), Tools for quality assessment of surface-based flux
917 measurements. *Agricultural and Forest Meteorology, 78*(1-2), 83-105. https://doi.org/Doi
918 10.1016/0168-1923(95)02248-1.
919 French, J., Oolman, L., & Plummer, D. (2021). *University of Wyoming King Air (UWKA) High*
920 *Rate Flight Level Data*. https://doi.org/10.26023/5B70-4VP5-XY0V.
921 Gao, Z. M., Liu, H. P., Russell, E. S., Huang, J. P., Foken, T., & Oncley, S. P. (2016), Large
922 eddies modulating flux convergence and divergence in a disturbed unstable atmospheric
923 surface layer. *Journal of Geophysical Research-Atmospheres, 121*(4), 1475-1492.
924 https://doi.org/10.1002/2015jd024529.
925 Garratt, J. (1994), Review: the atmospheric boundary layer. *Earth-Science Reviews, 37*(1-2), 89-
926 134. https://doi.org/10.1016/0012-8252(94)90026-4.
927 Haimov, S., & Rodi, A. (2013), Fixed-Antenna Pointing-Angle Calibration of Airborne Doppler
928 Cloud Radar. *Journal of Atmospheric and Oceanic Technology, 30*(10), 2320-2335.
929 https://doi.org/10.1175/Jtech-D-12-00262.1.
930 Halldin, S., Gryning, S. E., Gottschalk, L., Jochum, A., Lundin, L. C., & Van de Griend, A. A.
931 (1999), Energy, water and carbon exchange in a boreal forest landscape — NOPEX
932 experiences. *Agricultural and Forest Meteorology, 98-99*, 5-29.
933 https://doi.org/10.1016/s0168-1923(99)00148-3.
934 Helbig, M., Gerken, T., Beamesderfer, E. R., Baldocchi, D. D., Banerjee, T., Biraud, S. C., et al.
935 (2021), Integrating continuous atmospheric boundary layer and tower-based flux
936 measurements to advance understanding of land-atmosphere interactions. *Agricultural*
937 *and Forest Meteorology, 307*. https://doi.org/10.1016/j.agrformet.2021.108509.
938 Hill, T. C., Williams, M., & Moncrieff, J. B. (2008), Modeling feedbacks between a boreal forest
939 and the planetary boundary layer. *Journal of Geophysical Research, 113*(D15).
940 https://doi.org/10.1029/2007jd009412.
941 Hill, T. C., Williams, M., Woodward, F. I., & Moncrieff, J. B. (2011), Constraining ecosystem
942 processes from tower fluxes and atmospheric profiles. *Ecol Appl, 21*(5), 1474-1489.
943 https://doi.org/10.1890/09-0840.1.

Hu, X. M., Gourdji, S. M., Davis, K. J., Wang, Q., Zhang, Y., Xue, M., et al. (2021), Implementation of Improved Parameterization of Terrestrial Flux in WRF-VPRM Improves the Simulation of Nighttime CO2 Peaks and a Daytime CO2 Band Ahead of a Cold Front. *Journal of Geophysical Research: Atmospheres, 126*(10). https://doi.org/10.1029/2020jd034362.

Hu, X. M., Huang, Y., Xue, M., Martin, E., Hong, Y., Chen, M., et al. (2023), Effects of Lower Troposphere Vertical Mixing on Simulated Clouds and Precipitation Over the Amazon During the Wet Season. *Journal of Geophysical Research: Atmospheres, 128*(12). https://doi.org/10.1029/2023jd038553.

Kiemle, C., Brewer, W. A., Ehret, G., Hardesty, R. M., Fix, A., Senff, C., et al. (2007), Latent Heat Flux Profiles from Collocated Airborne Water Vapor and Wind Lidars during IHOP_2002. *Journal of Atmospheric and Oceanic Technology, 24*(4), 627-639. https://doi.org/10.1175/jtech1997.1.

LeMone, M. A., Angevine, W. M., Bretherton, C. S., Chen, F., Dudhia, J., Fedorovich, E., et al. (2019), 100 Years of Progress in Boundary Layer Meteorology. *Meteorological Monographs, 59*, 9.1-9.85. https://doi.org/10.1175/amsmonographs-d-18-0013.1.

Lin, G., Geerts, B., Wang, Z. E., Grasmick, C., Jing, X. Q., & Yang, J. (2019), Interactions between a Nocturnal MCS and the Stable Boundary Layer as Observed by an Airborne Compact Raman Lidar during PECAN. *Monthly Weather Review, 147*(9), 3169-3189. https://doi.org/10.1175/Mwr-D-18-0388.1.

Lin, G., Grasmick, C., Geerts, B., Wang, Z. E., & Deng, M. (2021), Convection Initiation and Bore Formation Following the Collision of Mesoscale Boundaries over a Developing Stable Boundary Layer: A Case Study from PECAN. *Monthly Weather Review, 149*(7), 2351-2367. https://doi.org/10.1175/Mwr-D-20-0282.1.

Lin, G., Wang, Z., Ziegler, C., Hu, X.-M., Xue, M., Geerts, B., & Chu, Y. (2023), A Comparison of Convective Storm Inflow Moisture Variability between the Great Plains and the Southeastern United States Using Multiplatform Field Campaign Observations. *Journal of Atmospheric and Oceanic Technology, 40*(5), 539-556. https://doi.org/10.1175/jtech-d-22-0037.1.

973 Linné, H., Hennemuth, B., Bösenberg, J., & Ertel, K. (2006), Water vapour flux profiles in the
974 convective boundary layer. *Theoretical and Applied Climatology, 87*(1-4), 201-211.
975 https://doi.org/10.1007/s00704-005-0191-7.
976 Liu, B., Wang, Z., Cai, Y., Wechsler, P., Kuestner, W., Burkhart, M., & Welch, W. (2014),
977 Compact airborne Raman lidar for profiling aerosol, water vapor and clouds. *Opt Express,*
978 *22*(17), 20613-20621. https://doi.org/10.1364/OE.22.020613.
979 Mahrt, L. (1998), Flux sampling errors for aircraft and towers. *Journal of Atmospheric and*
980 *Oceanic Technology, 15*(2), 416-429. https://doi.org/Doi 10.1175/1520-
981 0426(1998)015<0416:Fsefaa>2.0.Co;2.
982 Mahrt, L. (2000), Surface Heterogeneity and Vertical Structure of the Boundary Layer.
983 *Boundary-Layer Meteorology, 96*(1-2), 33-62. https://doi.org/10.1023/a:1002482332477.
984 Mahrt, L. (2010), Computing turbulent fluxes near the surface: Needed improvements.
985 *Agricultural and Forest Meteorology, 150*(4), 501-509.
986 https://doi.org/10.1016/j.agrformet.2010.01.015.
987 Margairaz, F., Pardyjak, E. R., & Calaf, M. (2020), Surface Thermal Heterogeneities and the
988 Atmospheric Boundary Layer: The Relevance of Dispersive Fluxes. *Boundary-Layer*
989 *Meteorology, 175*(3), 369-395. https://doi.org/10.1007/s10546-020-00509-w.
990 Mauder, M., Desjardins, R. L., & MacPherson, I. (2007), Scale analysis of airborne flux
991 measurements over heterogeneous terrain in a boreal ecosystem. *Journal of Geophysical*
992 *Research: Atmospheres, 112*(D13). https://doi.org/10.1029/2006jd008133.
993 Mauder, M., Foken, T., & Cuxart, J. (2020), Surface-Energy-Balance Closure over Land: A
994 Review. *Boundary-Layer Meteorology, 177*(2-3), 395-426.
995 https://doi.org/10.1007/s10546-020-00529-6.
996 Mauder, M., Jegede, O. O., Okogbue, E. C., Wimmer, F., & Foken, T. (2006), Surface energy
997 balance measurements at a tropical site in West Africa during the transition from dry to
998 wet season. *Theoretical and Applied Climatology, 89*(3-4), 171-183.
999 https://doi.org/10.1007/s00704-006-0252-6.
1000 Metzger, S., Durden, D., Paleri, S., Sühring, M., Butterworth, B. J., Florian, C., et al. (2021),
1001 Novel approach to observing system simulation experiments improves information gain
1002 of surface–atmosphere field measurements. *Atmospheric Measurement Techniques,*
1003 *14*(11), 6929-6954. https://doi.org/10.5194/amt-14-6929-2021.

Metzger, S., Junkermann, W., Mauder, M., Butterbach-Bahl, K., Trancón y Widemann, B., Neidl, F., et al. (2013), Spatially explicit regionalization of airborne flux measurements using environmental response functions. *Biogeosciences, 10*(4), 2193-2217. https://doi.org/10.5194/bg-10-2193-2013.

Oncley, S. (2021). *NCAR/EOL 5 minute ISFS surface flux data, tilt corrected, geographic coordinate winds*. https://doi.org/https://doi.org/10.26023/43MF-NP8N-3Q0V.

Orlanski, I. (1975), A rational subdivision of scales for atmospheric processes. *Bulletin of the American Meteorological Society, 56*(5), 527-534. https://doi.org/https://doi.org/10.1175/1520-0477-56.5.527.

Paleri, S., Desai, A. R., Metzger, S., Durden, D., Butterworth, B. J., Mauder, M., et al. (2022), Space-Scale Resolved Surface Fluxes Across a Heterogeneous, Mid-Latitude Forested Landscape. *Journal of Geophysical Research: Atmospheres, 127*(23). https://doi.org/10.1029/2022jd037138.

Pielke, R. A., Sr, Avissar, R., Raupach, M., Dolman, A. J., Zeng, X., & Denning, A. S. (2003), Interactions between the atmosphere and terrestrial ecosystems: influence on weather and climate. *Global Change Biology, 4*(5), 461-475. https://doi.org/10.1046/j.1365-2486.1998.t01-1-00176.x.

Platis, A., Moene, A. F., Villagrasa, D. M., Beyrich, F., Tupman, D., & Bange, J. (2017), Observations of the Temperature and Humidity Structure Parameter Over Heterogeneous Terrain by Airborne Measurements During the LITFASS-2003 Campaign. *Boundary-Layer Meteorology, 165*(3), 447-473. https://doi.org/10.1007/s10546-017-0290-x.

Pressel, K. G., Collins, W. D., & Desai, A. R. (2014), The spatial scale dependence of water vapor variability inferred from observations from a very tall tower. *Journal of Geophysical Research: Atmospheres, 119*(16), 9822-9837. https://doi.org/10.1002/2013jd021141.

Raupach, M. R., & Finnigan, J. J. (1995), Scale Issues in Boundary-Layer Meteorology - Surface-Energy Balances in Heterogeneous Terrain. *Hydrological Processes, 9*(5-6), 589-612. https://doi.org/DOI 10.1002/hyp.3360090509.

Sellers, P., Hall, F., Ranson, K. J., Margolis, H., Kelly, B., Baldocchi, D., et al. (1995), The Boreal Ecosystem–Atmosphere Study (BOREAS): An Overview and Early Results from

the 1994 Field Year. *Bulletin of the American Meteorological Society, 76*(9), 1549-1577. https://doi.org/10.1175/1520-0477(1995)076<1549:Tbesao>2.0.Co;2.

Steinfeld, G., Letzel, M. O., Raasch, S., Kanda, M., & Inagaki, A. (2007), Spatial representativeness of single tower measurements and the imbalance problem with eddy-covariance fluxes: results of a large-eddy simulation study. *Boundary-Layer Meteorology, 123*(1), 77-98. https://doi.org/10.1007/s10546-006-9133-x.

Stevens, B., & Bony, S. (2013), Water in the atmosphere. *Physics Today, 66*(6), 29-34. https://doi.org/10.1063/pt.3.2009.

Strunin, M. A., & Hiyama, T. (2005), Spectral Structure of Small-Scale Turbulent and Mesoscale Fluxes in the Atmospheric Boundary Layer over a Thermally Inhomogeneous Land Surface. *Boundary-Layer Meteorology, 117*(3), 479-510. https://doi.org/10.1007/s10546-005-2188-2.

Stull, R. (1988). *An introduction to boundary layer meteorology* (Vol. Vol.13): Springer Science & Business Media.

Stull, R. B. (2015), Practical Meteorology-An Algebra-based Survey of Atmospheric Science. *University of British Columbia*.

Sun, X.-M., Zhu, Z.-L., Wen, X.-F., Yuan, G.-F., & Yu, G.-R. (2006), The impact of averaging period on eddy fluxes observed at ChinaFLUX sites. *Agricultural and Forest Meteorology, 137*(3-4), 188-193. https://doi.org/10.1016/j.agrformet.2006.02.012.

Sun, Y., Jia, L., Chen, Q., Lin, X., Sude, B., Quan, Z., & Hutjes, R. W. A. (2023), Construction of a spatially gridded heat flux map based on airborne flux Measurements using remote sensing and machine learning methods. *Agricultural and Forest Meteorology, 334*. https://doi.org/10.1016/j.agrformet.2023.109424.

Thomas, C., & Foken, T. (2004), Detection of long-term coherent exchange over spruce forest using wavelet analysis. *Theoretical and Applied Climatology, 80*(2-4), 91-104. https://doi.org/10.1007/s00704-004-0093-0.

Torrence, C., & Compo, G. P. (1998), A Practical Guide to Wavelet Analysis. *Bulletin of the American Meteorological Society, 79*(1), 61-78. https://doi.org/10.1175/1520-0477(1998)079<0061:Apgtwa>2.0.Co;2.

1063 Vadrevu, K. P., & Choi, Y. (2011), Wavelet analysis of airborne CO2 measurements and related
1064 meteorological parameters over heterogeneous landscapes. *Atmospheric Research, 102*(1-
1065 2), 77-90. https://doi.org/10.1016/j.atmosres.2011.06.008.
1066 Wang, Z., Wechsler, P., Kuestner, W., French, J., Rodi, A., Glover, B., et al. (2009), Wyoming
1067 Cloud Lidar: instrument description and applications. *Optics Express, 17*(16), 13576-
1068 13587. https://doi.org/10.1364/OE.17.013576.
1069 Wolf, B., Chwala, C., Fersch, B., Garvelmann, J., Junkermann, W., Zeeman, M. J., et al. (2017),
1070 The SCALEX Campaign: Scale-Crossing Land Surface and Boundary Layer Processes in
1071 the TERENO-preAlpine Observatory. *Bulletin of the American Meteorological Society,*
1072 *98*(6), 1217-1234. https://doi.org/10.1175/bams-d-15-00277.1.
1073 Wu, D., Wang, Z., Wechsler, P., Mahon, N., Deng, M., Glover, B., et al. (2016), Airborne
1074 compact rotational Raman lidar for temperature measurement. *Opt Express, 24*(18),
1075 A1210-1223. https://doi.org/10.1364/OE.24.0A1210.
1076

Figure 1.

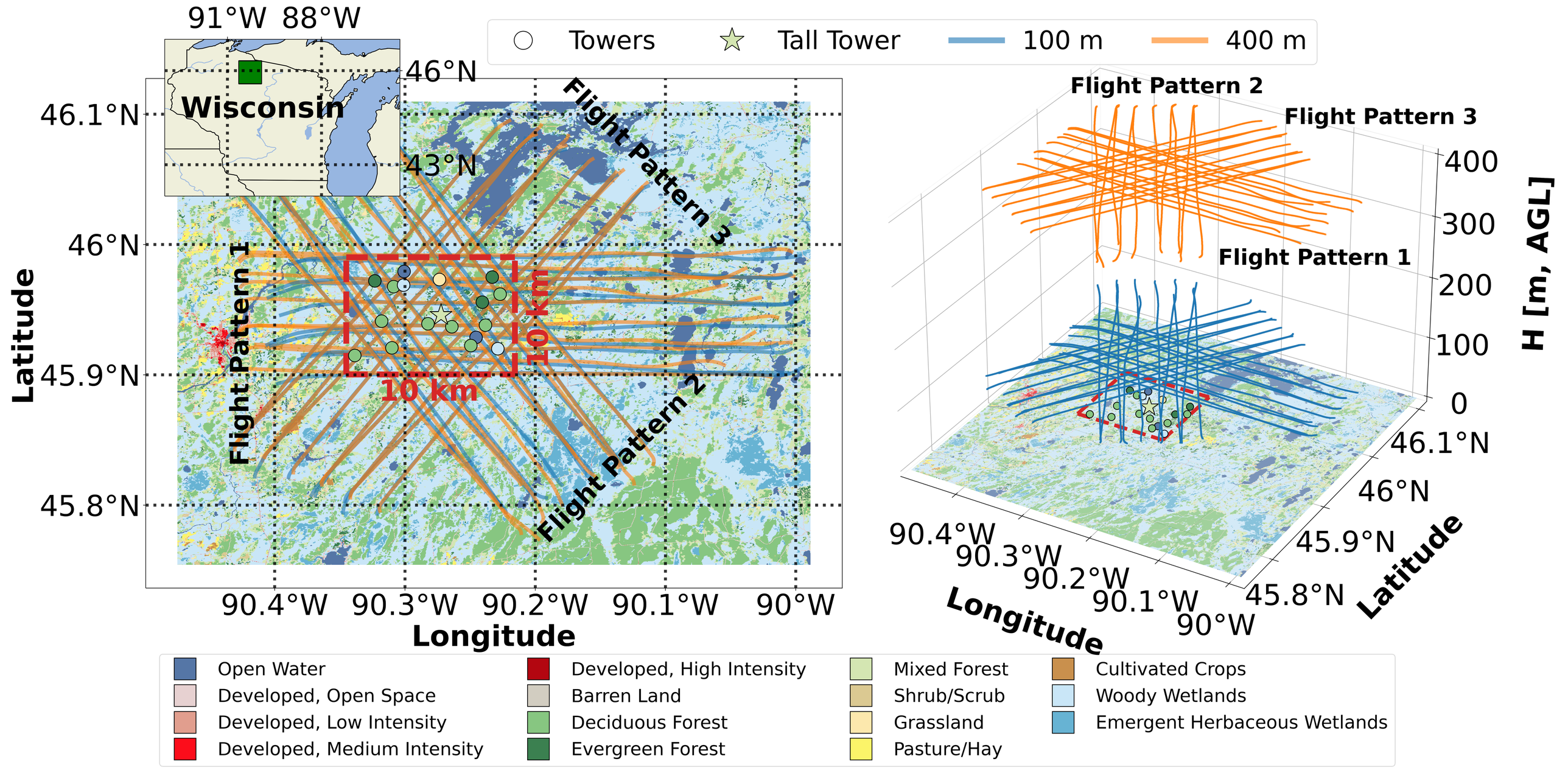
Towers
Tall Tower
100 m
400 m
Wisconsin
91°W
88°W
46°N
43°N
Flight Pattern 1
Flight Pattern 2
Flight Pattern 3
10 km
10 km
Latitude
Longitude
46.1°N
46°N
45.9°N
45.8°N
90.4°W
90.3°W
90.2°W
90.1°W
90°W
H [m, AGL]
400
300
200
100
0
Open Water
Developed, Open Space
Developed, Low Intensity
Developed, Medium Intensity
Developed, High Intensity
Barren Land
Deciduous Forest
Evergreen Forest
Mixed Forest
Shrub/Scrub
Grassland
Pasture/Hay
Cultivated Crops
Woody Wetlands
Emergent Herbaceous Wetlands

Figure 2.

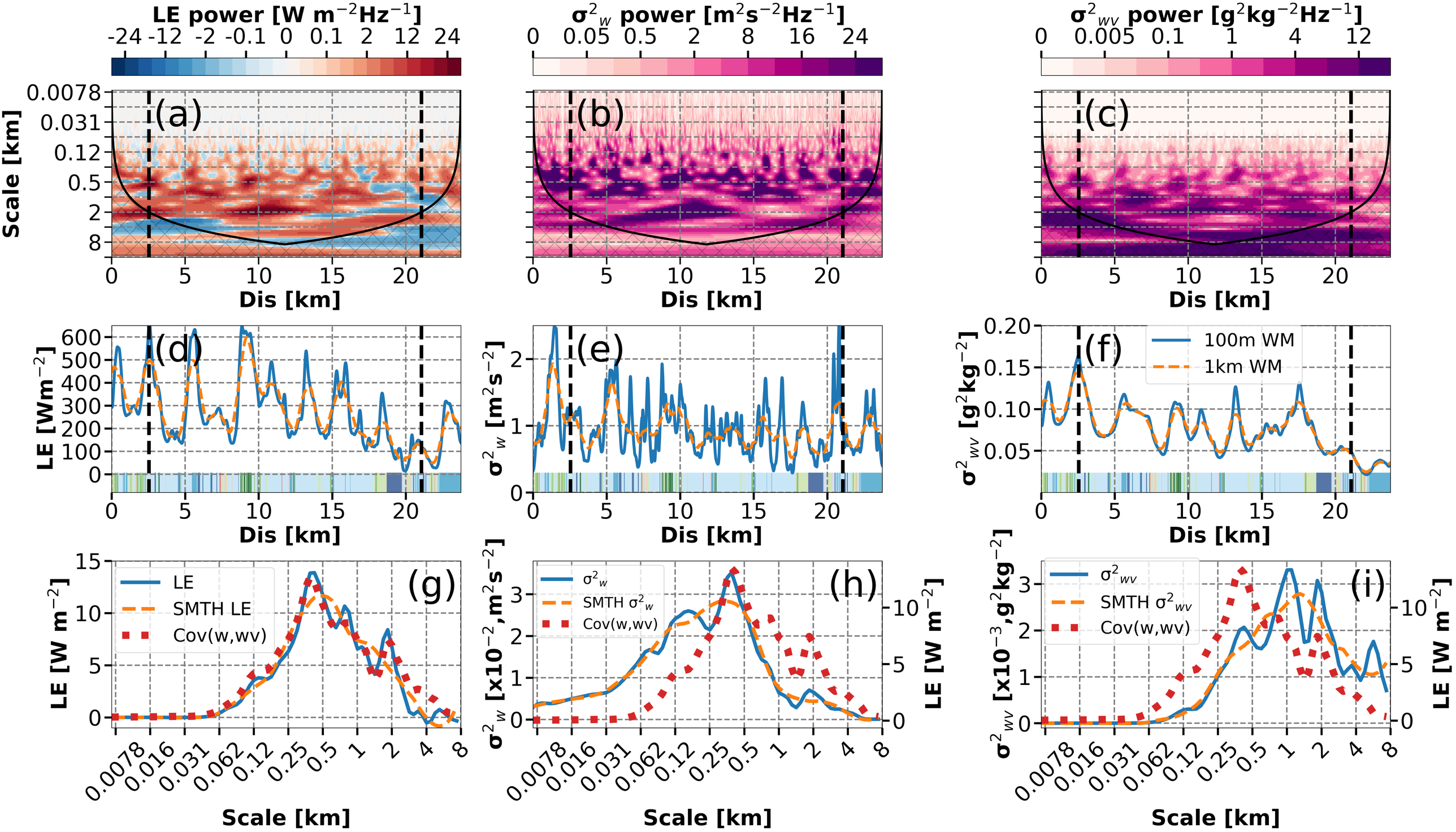
LE power [W m^{-2}Hz^{-1}]
-24 -12 -2 -0.1 0 0.1 2 12 24
σ^2_w power [m^{2}s^{-2}Hz^{-1}]
0 0.05 0.5 2 8 16 24
σ^2_{wv} power [g^{2}kg^{-2}Hz^{-1}]
0 0.005 0.1 1 4 12
Scale [km]
0.0078
0.031
0.12
0.5
2
8
(a)
(b)
(c)
Dis [km]
LE [Wm^{-2}]
σ^2_w [m^{2}s^{-2}]
σ^2_{wv} [g^{2}kg^{-2}]
(d)
(e)
(f)
100m WM
1km WM
LE [W m^{-2}]
σ^2_w [x10^{-2},m^{2}s^{-2}]
σ^2_{wv} [x10^{-3},g^{2}kg^{-2}]
LE
SMTH LE
Cov(w,wv)
σ^2_w
SMTH σ^2_w
σ^2_{wv}
SMTH σ^2_{wv}
(g)
(h)
(i)
Scale [km]

Figure 3.

(a)

MBE: 4.85 Wm^{-2} (3.2%)
RMSE: 24.41 Wm^{-2}
r^2: 0.915

Wavelet LE [$W\ m^{-2}$]

EC LE [$W\ m^{-2}$]

Probability

(b)

US-PFa 122m
FL Wavelet LE 100m
FL EC LE 100m

LE [$W\ m^{-2}$]

Hour [LT Since 9 July 00:00]

Figure 4.

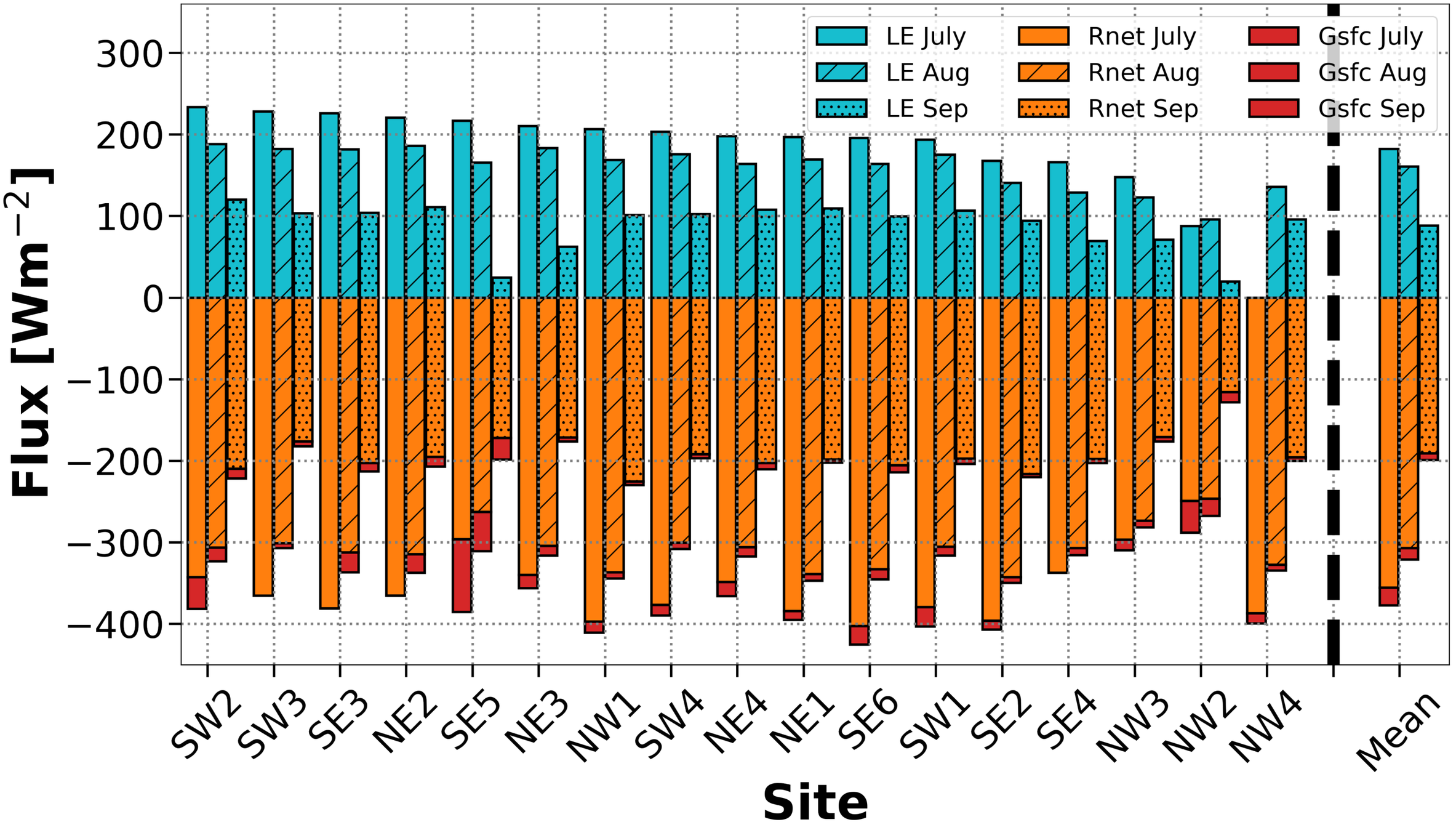
LE July
LE Aug
LE Sep
Rnet July
Rnet Aug
Rnet Sep
Gsfc July
Gsfc Aug
Gsfc Sep
300
200
100
0
−100
−200
−300
−400
Flux [Wm^{-2}]
SW2
SW3
SE3
NE2
SE5
NE3
NW1
SW4
NE4
NE1
SE6
SW1
SE2
SE4
NW3
NW2
NW4
Mean
Site

Figure 5.

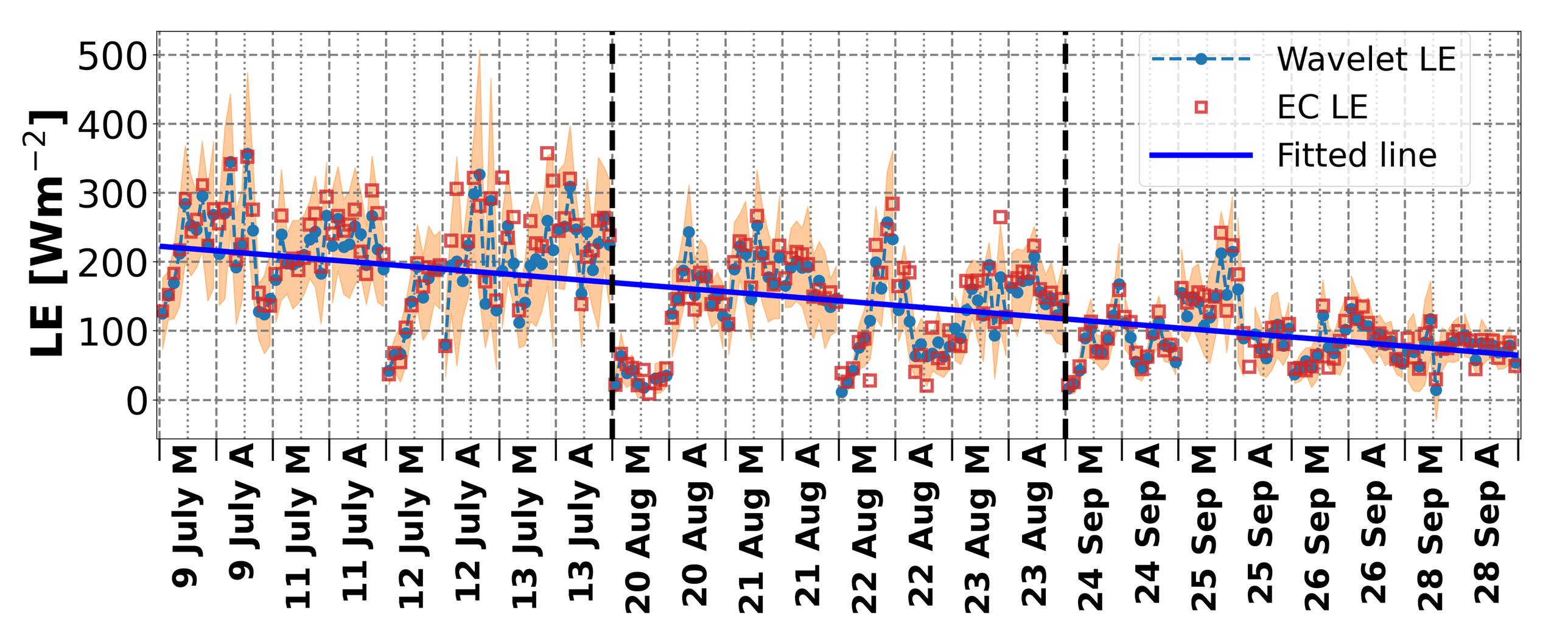
LE [Wm^{-2}]
500
400
300
200
100
0
Wavelet LE
EC LE
Fitted line
9 July M
9 July A
11 July M
11 July A
12 July M
12 July A
13 July M
13 July A
20 Aug M
20 Aug A
21 Aug M
21 Aug A
22 Aug M
22 Aug A
23 Aug M
23 Aug A
24 Sep M
24 Sep A
25 Sep M
25 Sep A
26 Sep M
26 Sep A
28 Sep M
28 Sep A

Figure 6.

Scale-Resolved LE [W m $^{-2}$]

−1.5 0.0 1.5 3.0 4.5 6.0 7.5 9.0 10.5 12.0

Scale-Integr LE [W m $^{-2}$]

0 100 200 300 400

(a) 9 July

(b) 11 July

(c) 12 July

(d) 13 July

(e) 20 Aug

(f) 21 Aug

(g) 22 Aug

(h) 23 Aug

(i) 24 Sep

(j) 25 Sep

(k) 26 Sep

(l) 28 Sep

Leg

2 4 6 8 10 12 14 16 18 20

Scale [km]

0.0078 0.016 0.031 0.062 0.12 0.25 0.5 1 2 4 8

Figure 7.

Scale-Integr σ^2_w [m^2s^{-2}]

Scale-Integr σ^2_{wv} [g^2kg^{-2}]

(a) (b) (c)

(d) (e) (f)

Scale-Integr LE [Wm^{-2}]

Scale-Integr

50% Cum Norm

(g) (h) (i)

Norm Value [$x10^{-2}$]

Cum Norm Value

Norm C1

Norm C2

Cum C1

Cum C2

Scale [km]

Norm LE [$x10^{-2}$]

Norm σ^2_w [$x10^{-2}$]

Norm σ^2_{wv} [$x10^{-2}$]

Scale-Resolved LE [$W\ m^{-2}$]

Scale-Resolved σ^2_w [$x10^{-3}$,m^2s^{-2}]

Scale-Resolved σ^2_{wv} [$x10^{-4}$,g^2kg^{-2}]

Figure 8.

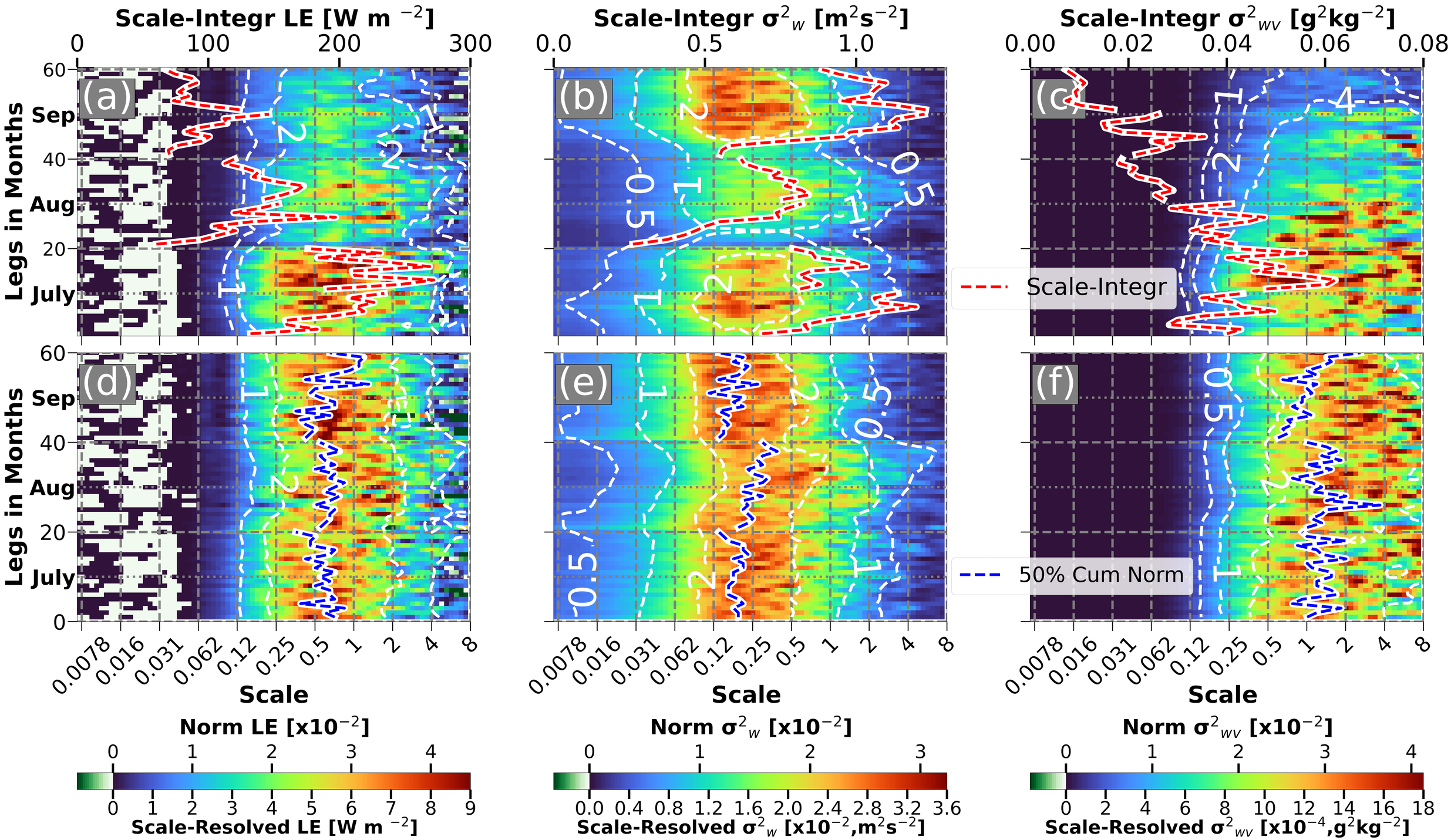
Scale-Integr LE [W m $^{-2}$]
Scale-Integr σ^2_w [m^{2}s^{-2}]
Scale-Integr σ^2_{wv} [g^{2}kg^{-2}]
(a)
(b)
(c)
(d)
(e)
(f)
Legs in Months
Sep
Aug
July
Scale
Scale-Integr
50% Cum Norm
Norm LE [x10^{-2}]
Scale-Resolved LE [W m $^{-2}$]
Norm σ^2_w [x10^{-2}]
Scale-Resolved σ^2_w [x10^{-2},m^{2}s^{-2}]
Norm σ^2_{wv} [x10^{-2}]
Scale-Resolved σ^2_{wv} [x10^{-4},g^{2}kg^{-2}]

Figure 9.

Percentage (%)
0 20 40 60 80
(a)
(b)
(c)
LE [W m $^{-2}$]
260 220 180 140 100 60 20
0 50 100 150 200 250
0.0 0.3 0.6 0.9
0.00 0.02 0.04 0.06
< 200m
200m - 2km
2km - 8km
< 200m
200m - 2km
2km - 8km
cov:<200m
cov:200m-2km
cov:2km-8km
(d)
(e)
(f)
Legs in Month
60 40 20 0
Sep
Aug
July
0 100 200
0.0 0.5 1.0
0.00 0.02 0.04 0.06
LE [W m $^{-2}$]
σ^2_w [m^{2}s^{-2}]
σ^2_{wv} [g^{2}kg^{-2}]

Figure 10.

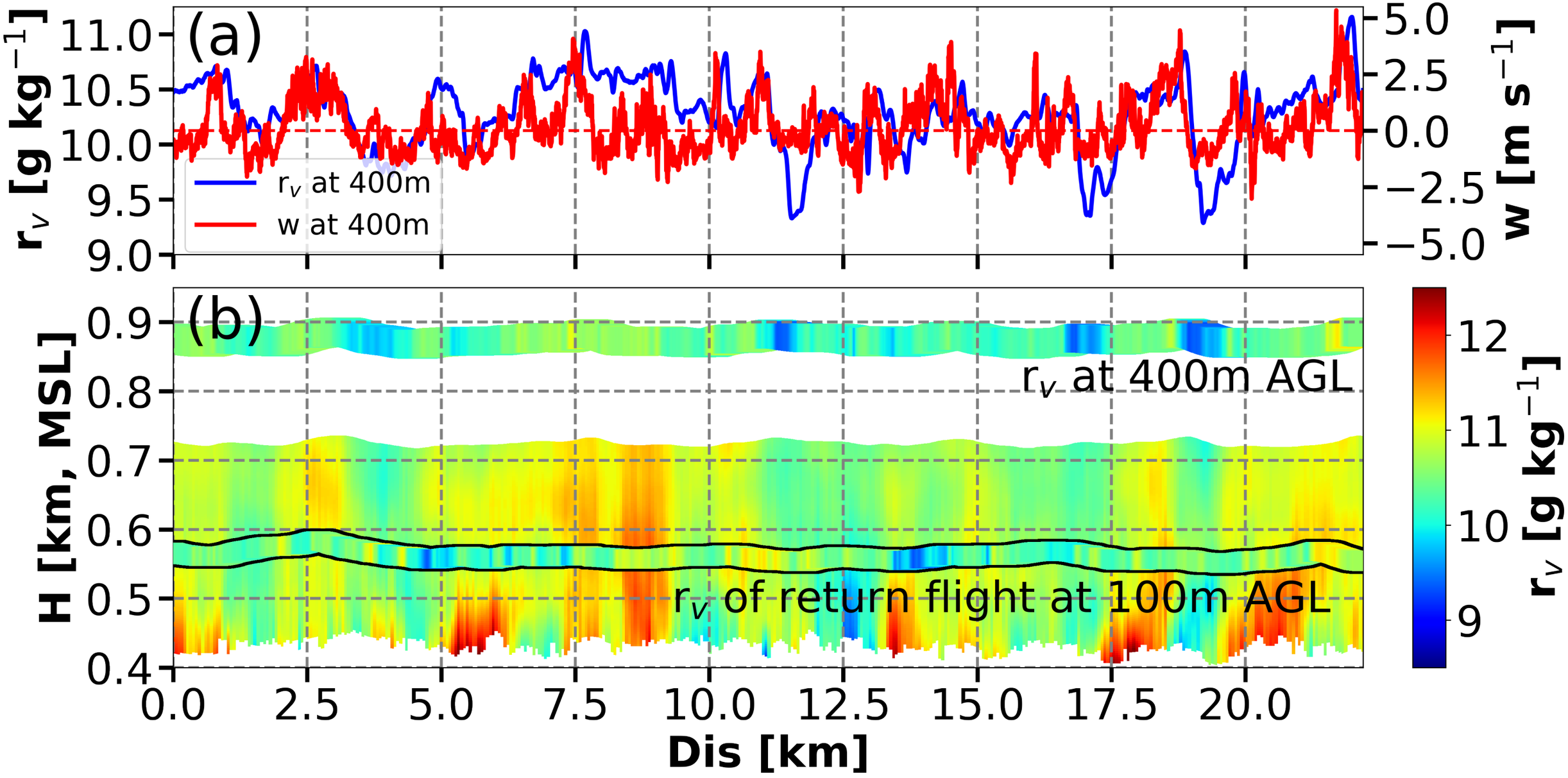
(a)
r_v [g kg^{-1}]
11.0
10.5
10.0
9.5
9.0
r_v at 400m
w at 400m
5.0
2.5
0.0
−2.5
−5.0
w [m s^{-1}]
(b)
H [km, MSL]
0.9
0.8
0.7
0.6
0.5
0.4
r_v at 400m AGL
r_v of return flight at 100m AGL
12
11
10
9
r_v [g kg^{-1}]
0.0
2.5
5.0
7.5
10.0
12.5
15.0
17.5
20.0
Dis [km]